

UC Berkeley

UC Berkeley Previously Published Works

Title

Hyperpolarized relaxometry based nuclear T_1 noise spectroscopy in diamond.

Permalink

<https://escholarship.org/uc/item/5763k8jk>

Journal

Nature communications, 10(1)

ISSN

2041-1723

Authors

Ajoy, A
Safvati, B
Nazaryan, R
et al.

Publication Date

2019-11-01

DOI

10.1038/s41467-019-13042-3

Peer reviewed

Hyperpolarized relaxometry based nuclear T_1 noise spectroscopy in diamond

A. Ajoy,¹ B. Safvati,¹ R. Nazaryan,¹ J. T. Oon,¹ B. Han,¹ P. Raghavan,¹ R. Nirodi,¹ A. Aguilar,¹ K. Liu,¹ X. Cai,¹ X. Lv,¹ E. Druga,¹ C. Ramanathan,² J. A. Reimer,³ C. A. Meriles,⁴ D. Suter,⁵ and A. Pines¹

¹*Department of Chemistry, and Materials Science Division Lawrence Berkeley National Laboratory University of California, Berkeley, California 94720, USA.*

²*Department of Physics and Astronomy, Dartmouth College, Hanover, New Hampshire 03755, USA.*

³*Department of Chemical and Biomolecular Engineering, and Materials Science Division Lawrence Berkeley National Laboratory University of California, Berkeley, California 94720, USA.*

⁴*Department of Physics and CUNY-Graduate Center, CUNY-City College of New York, New York, NY 10031, USA.*

⁵*Fakultät Physik, Technische Universität Dortmund, D-44221 Dortmund, Germany.*

Understanding the origins of spin lifetimes in quantum systems is a matter of current importance in several areas of quantum information and sensing. Methods that spectrally map spin relaxation processes provide insight into their origin and can motivate methods to mitigate them. In this paper, using a combination of hyperpolarization and precision field cycling over a wide range (1 mT - 7 T), we map frequency dependent relaxation in a prototypical system of ^{13}C nuclear spins in diamond coupled to Nitrogen Vacancy electronic centers. Nuclear hyperpolarization through the optically pumped NV electrons allows signal time savings for the measurements exceeding million-fold over conventional methods. We observe that ^{13}C lifetimes show a dramatic field dependence, growing rapidly with field up to ~ 100 mT and saturating thereafter. Through a systematic study with increasing substitutional electron (P1 center) concentration as well as ^{13}C enrichment levels, we identify the operational relaxation channels for the nuclei in different field regimes. In particular, we demonstrate the dominant role played by the ^{13}C nuclei coupling to the interacting P1 electronic spin bath. These results pave the way for quantum control techniques for dissipation engineering to boost spin lifetimes in diamond, with applications ranging from engineered quantum memories to hyperpolarized ^{13}C imaging, and more broadly to relaxation studies in hybrid quantum systems.

Introduction: – The power of quantum technologies, especially those for information processing and metrology, relies critically on the ability to preserve the fragile quantum states that are harnessed in these applications [1]. Indeed noise serves as an encumbrance to practical implementations, causing both decoherence as well as dissipation of the quantum states [2, 3]. Precise *spectral* characterization of the noise opens the door to strategies by which it can be effectively suppressed [4, 5] – case in point being the emergence of dynamical decoupling techniques that preserve quantum coherence by periodic driving [6]. In these cases, quantum control sets up a filter that decouples components of noise except those resonant with the exact filter period [7], allowing spectral decomposition of the *dephasing* noise afflicting the system. Experimentally implemented in ion traps [8], superconducting qubits [9] and solid-state NMR [10], this has spurred development of Floquet engineering to enhance T_2 decoherence times by over an order of magnitude in these physical quantum device manifestations [11–13].

Methods that analogously spectrally fingerprint T_1 relaxation processes, on the other hand, are more challenging to implement experimentally. If possible however, they could reveal the origins of relaxation channels, and foster means to suppress them. Applications to real-world quantum platforms are pressing: relaxation in Josephson junctions and ion trap qubits, for instance, occur due to often incompletely understood interactions with surface paramagnetic spins [14]. Relaxation studies are also important in the context of coupled quantum systems, such as those built out of electronic and nuclear spins. In the case of diamond Nitrogen Vacancy (NV) center electronic qubits coupled to ^{13}C nuclei [15], for instance, a detailed understanding of nuclear relaxation can have important implications for quantum sensing [16]: engineered NV- ^{13}C clusters form building blocks of quantum networks [17], are the basis for spin gyroscopes [18], and are harnessed as quantum memories in high-resolution nano-MRI probes [19]. Nuclear T_1 lifetimes are not dominated by phonon interactions, but instead are set by couplings with the intrinsic electronic spin baths themselves – a complex dynamics that is often difficult to probe exper-

imentally. Indeed only a small proportion of ^{13}C spins can be addressed or readout via the NV centers, as also the direct inductive readout of these spins suffer from extremely weak signals. Moreover, as opposed to T_2 noise spectroscopy carried out in the rotating frame [13], probing of T_1 processes have to be performed in the laboratory frame. This necessitates the ability to probe relaxation behavior while subjecting samples to widely varying magnetic field strengths.

In this paper, we develop a method of “*hyperpolarized relaxometry*” that overcomes these instrumental and technical challenges. We measure T_1 relaxation rates of ^{13}C spins in diamond samples relevant for quantum sensing with a high density of NV centers. Our T_1 noise spectroscopy proceeds with high resolution and over four decades of noise spectral frequency, revealing the physical origins of the relaxation processes. While experiments herein are demonstrated for ^{13}C spins in electron-rich diamond, these results are potentially more widely reflective of relaxation processes operational in other systems, including Si:P [20], wide bandgap materials such as SiC [21, 22], and diamond-based quantum simulator platforms constructed out of 2D materials such as graphene and hBN [23–25]. These results are also pertinent for producing and maintaining polarization in hyperpolarized solids, for applications employing hyperpolarized nanoparticles of Si or diamond as MRI tracers [26, 27], and in the relayed optical DNP of liquids mediated through nanodiamonds [28], since in these applications T_1 relaxation bounds the achievable polarization levels.

Key to our technique is the hyperpolarization of ^{13}C nuclei at room temperature, allowing the rapid and direct measurement of nuclear spin populations via bulk NMR [28]. Dynamic nuclear polarization (DNP) is carried out by optical pumping and polarizing the NV electrons to macroscopically large values ($>37\%$) and subsequently transferring this ^{13}C nuclei (Fig. 1A). This routinely leads to nuclear polarization levels $\gtrsim 0.5\%$. In a high-field (7 T) NMR detection spectrometer, for instance, the signals are enhanced by factors exceeding $\varepsilon \sim 300$ -800 times the Boltzmann value [28], boosting measurement times by 10^5 - 10^6 , and resulting in high single shot detection SNRs. This permits T_1 spectroscopy

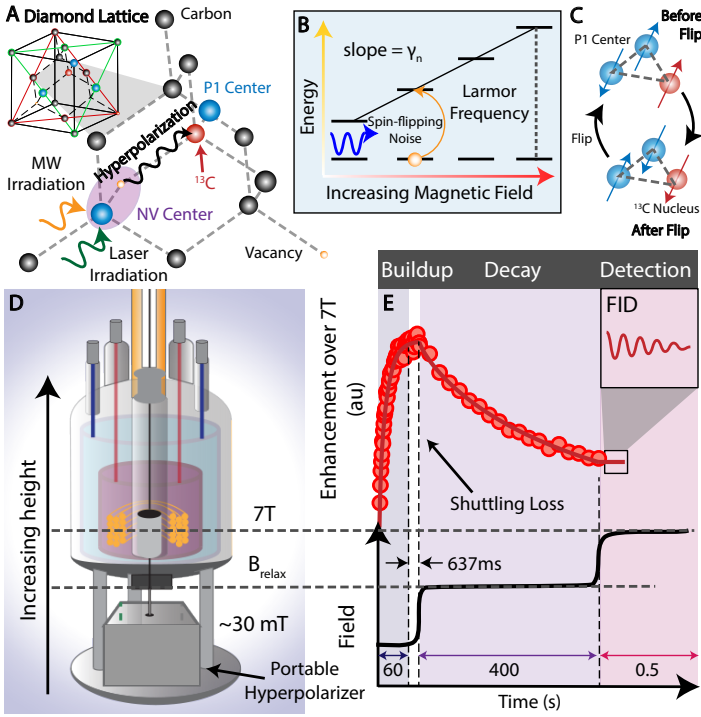


Figure 1. Principle. (A) System consisting of ^{13}C nuclear spins in diamond hyperpolarized via NV centers allowing their direct measurement by bulk NMR. Lattice also contains electronic spin bath of P1 centers. (B) Changing magnetic field allows probing of spin flipping noise that is resonant with the carbon Larmor frequency. (C) Dominant T_1 relaxation mechanism via three-body flip-flops with pairs of P1 center electrons. (D) Experimental platform. Portable hyperpolarizer is installed in a rapid field cycling device capable of sweeping between 10 mT - 7 T in the fringe field of a NMR magnet. (E) Time sequence. Lower panel shows the schematic steps of laser driven optical ^{13}C hyperpolarization for ~ 60 s at $B_{\text{pol}} \approx 30$ mT, rapid shuttling (< 1 s) to the field of interest B_{relax} , relaxation and subsequent high field detection at 7 T. Upper panel displays typical data for $200 \mu\text{m}$ microdiamond powder, where $B_{\text{relax}} = 2$ T. ^{13}C NMR signal amplitude (points) is quantified by its enhancement over the 7 T Boltzmann signal. Signal growth and decays are fitted to stretched exponentials (solid lines).

experiments that would have otherwise been intractable. Hyperpolarization is equally efficiently generated in single crystals as well as randomly oriented diamond powders, and both at natural abundance as well as enriched ^{13}C concentrations. The hyperpolarized samples are interfaced to a home built field cycler instrument [29] (see Fig. 1D and video in [30]) that is capable of rapid and high-precision changes in magnetic field over a wide 1 mT - 7 T range (extendable in principle from 1 nT - 7 T), opening a unique way to peer into the origins of nuclear spin relaxation.

^{13}C Hyperpolarized relaxometry: – Fig. 1D-E schematically describe the experiment. Hyperpolarization in the ^{13}C nuclei is affected by optical pumping at low fields, typically $B_{\text{pol}} \sim 40$ mT, followed by rapid transfer to the intermediate field B_{relax} where the spins are allowed to thermalize (see Fig. 1C), and subsequent bulk inductive measurement at 7 T. Experimentally varying B_{relax} allows one to probe field dependent lifetimes $T_1(B_{\text{relax}})$, and through them noise sources perpendicular to $\mathbf{B}_{\text{relax}}$ and resonant with the nuclear Larmor frequency $\gamma_n B_{\text{relax}}$ (Fig. 1B). Here $\gamma_n = 10.7$ MHz/T is the ^{13}C gyromagnetic ratio. This allows the spectral decomposition of noise processes that spawn T_1 relaxation. For instance pairs of substitutional nitrogen impurities (P1 centers) undergoing flip-flops (Fig. 1C) can apply on the ^{13}C

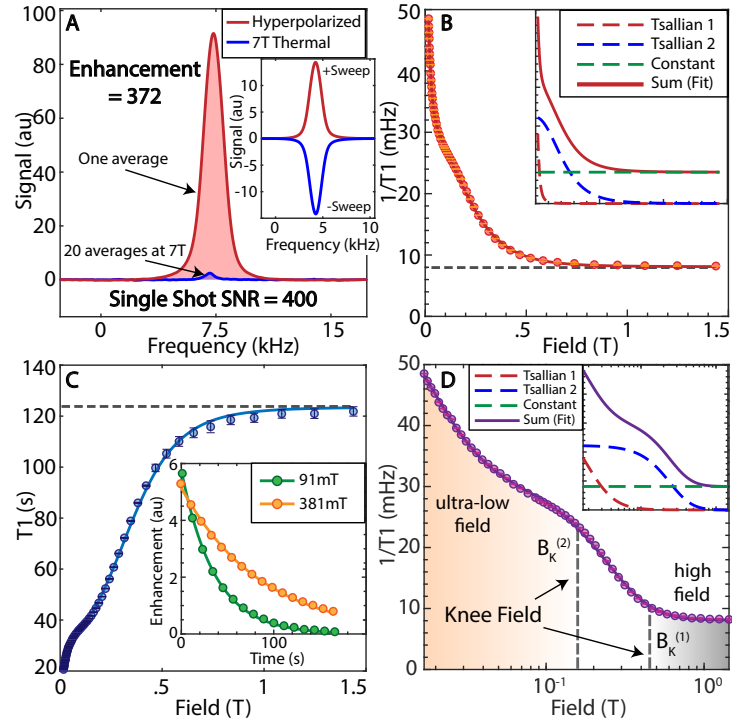


Figure 2. Hyperpolarized relaxometry applied to a 10% ^{13}C enriched single crystal (Sample 6 in Table I.). (A) Signal gains due to hyperpolarization under optimal conditions at $B_{\text{pol}} \approx 36$ mT. Red line shows a single-shot hyperpolarized signal (SNR ≈ 400) after 60 s of optical pumping. Blue line is the 7 T thermal signal after 20 averages, allowing us to quantify signal enhancement from DNP ≈ 372 over 7 T, a time saving by $\approx 10^6$ for equal SNR. Inset: Exemplary signals at $B_{\text{pol}} \approx 36$ mT under low-to-high (high-to-low) frequency sweeps leading to positive (negative) ^{13}C hyperpolarization. (B) Relaxation rate $R_1 = 1/T_1$ obtained from relaxometry over a wide field range 20 mT - 1.5 T. We observe a rapid growth in relaxation rate below a knee field of 0.5 T, and saturation at higher fields. Inset: Data can be fit to two Tsallian functions, which we ascribe to be originating from inter- ^{13}C couplings and interactions to the P1 spin bath. (C) Spin lifetimes as a function of field, showing significant boost in nuclear T_1 beyond the knee field, approaching a lifetime ≈ 2.1 min. Inset: Typical relaxation data at two representative fields showing monoexponential character. (D) Logarithmic scale data visualization, displaying a more equanimous sampling of experimental points, and the knee fields inflection points $B_K^{(1,2)}$. Inset: Decomposition into the constituent Tsallians. Error bars in all panels are obtained from monoexponential fits.

nuclei a stochastic spin-flipping field that constitutes a relaxation process.

Optical excitation for hyperpolarization involves 520 nm irradiation at low power (~ 80 mW/mm 2) applied continuously for ~ 40 s. Microwave (MW) sweeps, simultaneously applied across the NV center ESR spectrum, transfer this polarization to the ^{13}C spins (see Fig. 2A) [28, 33]. The hyperpolarization is carried out at room temperature, with the samples immersed under water, and at the relatively low optical power densities we employ, we do not observe sample heating (temperature < 100 C). DNP occurs in a manner that is completely independent of crystallite orientation. All parts of the underlying NV ESR spectrum produce hyperpolarization, with intensity proportional to the underlying electron density of states. The polarization sign depends solely on the direction of MW sweeps through the NV ESR spectrum (see Fig. 2A inset). Physically, hyperpolarization arises from partly adia-

Sample #	[P1] (ppm)	[NV] (ppm)	[¹³ C] (%)	Particulars	Growth
1	17 ± 2	1.4 ± 0.2	1.1	S.C.	HPHT
2	48 ± 6	6.9 ± 0.8	1.1	S.C.	HPHT
3	~200	~1-5	1.1	200 μm P	HPHT
4	~200	~1-5	1.1	5 μm P	HPHT
5	~200	1-10	3	S.C.	CVD
6	~200	1-10	10	S.C.	CVD
7	~200	1-10	100	S.C.	CVD

Table I. **Summary of samples and their defining characteristics.** We consider single-crystal (S.C.) samples both at natural abundance and with ¹³C enrichment, as well as diamond particulate (P) samples. Samples are grown either by high pressure high temperature (HPHT) or chemical vapor deposition (CVD). Colors refer to samples prepared under electron irradiation conditions by the same manufacturer (see Refs. [31, 32] for sample characterization data).

batic traversals of a pair of Landau-Zener (LZ) crossings in the rotating frame that are excited by the swept MWs. For a more detailed exposition of the DNP mechanism, we point the reader to Ref. [34].

Low field hyperpolarization is hence excited independent of the fields B_{relax} under which relaxation dynamics is to be studied. There is significant acceleration in acquisition time since optical DNP obviates the need to thermalize spins at high fields where T_1 times can be long (for some samples >30min). Gains averaging time are $\approx \varepsilon^2 \frac{T_1(7T)}{T_1(B_{\text{pol}})}$, which in our experimental conditions exceeds five orders of magnitude. In Fig. 2A for instance on a 10% enriched single crystal, we obtain large DNP enhancements $\varepsilon = 380$, and high single shot SNR ≈ 400 . It also reflects the inherently high DNP efficiency: every NV center has surrounding it $\sim 10^5$ nuclear spins, which we polarize to a bulk value (averaged over all ¹³C nuclei) of 0.37% employing just 3000 MW sweeps, indicating a transfer efficiency of $\approx 12.3\%$ per sweep per fully polarized nuclear spin. Harnessing this large signal gain allows us to perform relaxometry at a density of field points that are about two orders of magnitude greater than previous efforts [35–37]. Such high-resolution spectral mapping (for instance 55 field points in Fig. 2) can transparently reveal the underlying processes driving nuclear relaxation. Indeed, in future work, use of small flip-angle pulses might allow one to obtain the entire relaxation curve with a single round of DNP, and thus the *ultrafast relaxometry* of the nuclei.

Our experiments are also aided by technological attributes of the DNP mechanism. DNP is carried out under low fields and laser and MW powers, and allows construction of a compact hyperpolarizer device that can accessorize a field cycling instrument [38] (see [39] for video of hyperpolarizer operation). The wide range (1 mT - 7 T) field cyclers is constructed over the 7 T detection magnet, and affects rapid magnetic field changes by physically transporting the sample in the axial fringe field environment of the magnet [29]. This is accomplished by a fast (2 m/s) conveyor belt actuator stage (Parker HMRB08) that *shuttles* the sample via a carbon fiber rod (see video in Ref. [30]). The entire sample (field) trajectory can be programmed, allowing implementation of the polarization, relaxation and detection periods as in Fig. 1E. Transfer times at the maximum travel range were measured to be 648 ± 4 ms [40], short in comparison with the T_{1n} lifetimes we probe. High positional resolution (50 μm) allows access to field steps at high precision ([40] shows full field-position map). The field is primarily in the \hat{z} direction (parallel to the detection magnet), since sample transport occurs centrally, and the diameter of

the shuttling rod (8mm) is small in comparison with the magnet bore (54 mm). This ensures that the spatial gradients of the magnetic field, both longitudinally, as well as transverse, are negligible (under 1% of the bias field) (see [40]).

Results: – In this paper, we perform T_1 noise spectroscopy on ¹³C nuclei in a variety of diamond samples outlined in Table I. Fig. 2 shows representative results, considering here a 10% enriched single crystal (Sample 6). This intriguing data can be visualized in several complementary ways. First, considering relaxation rate $R_1 = 1/T_1$ (Fig. 2B), the high-resolution data allows us to clearly discern three regimes: a steep narrow R_1 increase at ultralow fields (<10 mT), a broader component at moderate fields (10 mT - 500 mT), and an approximately constant relaxation rate independent of field beyond 0.5 T and extending upto 7 T (data beyond 2 T not shown). Each point in Fig. 2B reports the monoexponential decay constant obtained from the *full* decay curve at every field value (for example shown in Fig. 2C). Error bars at each field value are estimated from monoexponential fits of the polarization decays. The resulting errors are under a few percent. The solid line in Fig. 2B indicates a numerical fit and remarkably closely follows the experimental data. Here we employ a sum of two Tsallian functions [41, 42] that capture the decay rates at low and moderate fields, and a constant offset at high field (see Fig. 2B insets).

A second viewpoint of the data, presented in Fig. 2C, is of the T_1 relaxation times and highlights its highly nonlinear field dependence. There is a *step-like* behavior in $T_1(B_{\text{relax}})$, and an inflection point (*knee* field) ≈ 100 mT beyond which the T_1 's saturate. We quantify the knee field value, $B_K^{(1)}$, as the B_{relax} at which the relaxation rate is twice the saturation R_1 that we observe at high field. This somewhat counterintuitive dependence has significant technological implications. (i) Long ¹³C lifetimes can be fashioned even at relatively modest fields at room temperature. This adds value in the context of ¹³C hyperpolarized nanodiamonds as potential MRI tracers [43], since it provides enough time for the circulation and binding of surface functionalized particles to illuminate disease conditions. (ii) The step-behavior in Fig. 2C also would prove beneficial for ¹³C hyperpolarization storage and transport. Exceedingly long lifetimes can be obtained by simply translating polarized diamond particles to modest ~ 100 mT fields – low enough to be produced by simple permanent magnets [38].

Finally, while the visualizations in Fig. 2B,C cast light on the low and high field behaviors respectively, the most natural representation of the wide-field data is on a logarithmic scale (Fig. 2D). The high-density data now unravels the rich relaxation behavior at play in the different field regimes. We discern an additional second inflection point $B_K^{(2)}$ at lower magnetic fields below which there is a sudden increase in the relaxation rates. The inset in Fig. 2D shows the decomposition into constituent Tsallian fits with a narrow and broad widths.

Microscopic origins of this relaxation behavior can be understood by first considering the diamond lattice to consist of three disjoint spin *reservoirs* – electron reservoirs of NV centers, P1 centers, and the ¹³C nuclear spin reservoir. P1 centers arise predominantly during NV center production on account of finite conversion efficiency in the diamond lattice. Indeed the P1 centers are typically at 10-100 times higher concentration than NV centers; with typical lattice concentrations of NVs, P1s and ¹³C nuclei respectively $P_{\text{NV}} \sim 1$ ppm, $P_e \sim 10$ -100 ppm, and $P_C \sim 10^4 \eta$ ppm, where η is the ¹³C lattice enrichment level. At any non-zero field of interest (ignoring level anti-crossings to aligned NV centers at 100mT), B_{relax} , the electron and nuclear reservoirs are centered at

widely disparate frequencies and do not overlap. We can separate the relaxation processes in different field regimes to be driven respectively by – (i) couplings of ^{13}C nuclei to pairs (or generally the reservoir) of P1 centers. This leads to the $B_K^{(1)}$ feature at moderate fields in Fig. 2D; (ii) ^{13}C spins interacting with individual P1 or NV centers undergoing lattice driven relaxation (T_{1e} processes); (iii) inter-nuclear couplings within the ^{13}C reservoir that convert Zeeman order to dipolar order. Both of latter processes contribute to the low field $B_K^{(2)}$ features in Fig. 2D; and finally, (iv) a high-field process $>1\text{T}$ that shows a slowly varying (approximately constant) field profile. We ascribe this to arise directly or indirectly (via electrons) from two-phonon Raman processes. Since these individual mechanisms are independent, the overall relaxation rate is obtained through a sum, $\frac{1}{T_1} = \sum_{(J)} \frac{1}{T_1^{(J)}}$ (shown in the inset of Fig. 2D).

Effect of electronic spin bath: – Let us first experimentally consider the relaxation process stemming from ^{13}C spins coupling to the interacting P1 reservoir. While lattice other paramagnetic defects, e.g. V^- , N3 and H3 centers [44, 45] are also likely present, they occur at much reduced concentration than the P1 centers, and their effects to ^{13}C relaxation indistinguishable from the P1s. In Fig. 3 we consider single crystal samples of natural ^{13}C abundance grown under similar conditions but with different nitrogen concentrations (Samples 1-2 in Table I). Their P1 electron concentrations are $P_e = 17$ ppm and $P_e = 48$ ppm respectively, and were measured from X-band ESR [46] shown in Fig. 3A (inset). To obtain data with high density of field-points, hyperpolarized relaxometry measurements are taken by an accelerated strategy (outlined in [40]) over a ultra-wide field range from 1 mT - 7T, with DNP being excited at $B_{\text{pol}}=36$ mT. For relaxometry at fields below B_{pol} , we employ rapid current switching of Helmholtz coils within the hyperpolarizer device. Both the range of fields, as well as the density of field-points being probed are significantly higher than previous studies [35, 47]. This aids in quantitatively unraveling the underlying physics of the relaxation processes. We note that probing relaxation behavior below ~ 1 mT in our experiments is currently limited by the finite sample shuttling time, which becomes of the order of the T_1 's being probed.

Experimental results in Fig. 3 reveal a remarkably sharp R_1 dependence, best displayed in Fig. 3A on a logarithmic scale, showing variation in relaxation rate over four orders of magnitude. Each curve fits to a sum of two Tsallian functions (solid line), and reveals the $B_K^{(1)}$ inflection point (closely resembling Fig. 2B) beyond which the lifetimes saturate. The second knee field $B_K^{(2)}$ at ultralow fields can also be discerned, although determining its exact position is difficult without relaxation data approaching truly zero-field. Comparing the two samples (Fig. 3A), we observe a clear correlation in the $B_K^{(1)}$ knee field values shifting to higher fields at higher electron concentration P_e . The high field relaxation rates, highlighted in Fig. 3B, increase with P_e . Interestingly at low fields (see Fig. 3C), the diamond with lower P_e (Sample 1) has an enhanced relaxation rate, yielding an apparent ‘‘cross-over’’ in the relaxation data between the two samples at ≈ 50 mT.

While we have focused here on single crystals, we observe quantitatively identical relaxation behavior also for microdiamond powders (eg. Samples 3-4 in Table I), down to $5 \mu\text{m}$ sizes (see Fig. 4). Indeed hyperpolarized particulate samples have a potentially wider application space, both as polarization agents and contrast agents in MRI, and the results indicate that the random orientations of the crystallites play no significant role in the dominant

P1-driven nuclear relaxation process. We do expect, however, that for nanodiamond particles <100 nm, surface electronic spins will cause an additional relaxation channel.

Let us now develop a simple model to quantify this P1-dominated relaxation process. Given the low relative density of the NV centers and consequently weak NV-NV couplings, to a good approximation they play no role except to inject polarization into the ^{13}C nuclei. Consider the Hamiltonian of the system, assumed for simplicity to be a single ^{13}C spin, and the environment - the interacting bath of P1 centers surrounding it, $\mathcal{H} = \mathcal{H}_S + \mathcal{H}_E + \mathcal{H}_{SE} + \mathcal{H}_{EE}$ where, the first two terms capture the Zeeman parts, the third term is the coupling between reservoirs, and the last term captures the inter-electron dipolar couplings within the P1 bath. Specifically,

$$\mathcal{H} = \omega_L I_z + \omega_e S_z + \sum_j A_{zx}^j S_{zj} I_x + \sum_{j < k} d_{jk}^{ee} \left[S_{zj} S_{zk} + \frac{1}{2} (S_j^+ S_k^- + S_j^- S_k^+) \right]. \quad (1)$$

where I (and S) refer to spin- $\frac{1}{2}$ Pauli operators on the nuclei (electrons) respectively, and A_{zx}^j the pseudo-secular hyperfine interaction that can drive nuclear spin-flips on the ^{13}C nuclei. For simplicity, we neglect here the effect of the P1 hyperfine couplings to host ^{14}N nuclei. In principle, they just split the electronic reservoirs seen by the ^{13}C nuclei into three manifolds separated by the large hyperfine coupling $A_{\parallel}^{\text{P1}} \approx 114\text{MHz}$. In the rotating frame at \mathcal{H}_E , and going into an interaction picture with respect to \mathcal{H}_{EE} , the Hamiltonian becomes, $\mathcal{H}_I = \omega_L I_z + \langle A_{zx} \rangle I_x \sum_j \left(e^{-i\mathcal{H}_{EE}t} \hat{S}_z e^{i\mathcal{H}_{EE}t} \right) = \omega_L I_z + \langle A_{zx} \rangle \hat{S}_z(t) I_x$ with, $\langle A_{zx} \rangle = \sqrt{\langle A_{zx}^2 \rangle} = \left[\sum_j (A_{zx}^j)^2 \right]^{1/2}$ and the operator $\hat{S}_z = \frac{1}{\langle A_{zx} \rangle} \sum_j A_{zx}^j S_{zj}$. Here $\langle A_{zx} \rangle$ is the total effective P1- ^{13}C hyperfine interaction, and the norm $\|\mathcal{H}_{EE}\|$ is set by the average dipolar interaction between electronic spins in the bath, henceforth $\langle d_{ee} \rangle$. We now make a semi-classical approximation, promoting \hat{S}_z to $s_z(t)$, a variable that represents a classical stochastic process seen by the ^{13}C nuclear spins [10, 48],

$$\mathcal{H}_I = \omega_L I_z + \langle A_{zx} \rangle s_z(t) I_x. \quad (2)$$

In summary therefore, a spin flipping term I_x is tethered to a stochastic variable $s(t)$ and this serves as ‘‘noise’’ on the ^{13}C spins, flipping them at random instances, resulting in nuclear relaxation upon a time (or ensemble) average. Interestingly, this noise process arises due to electronic flip-flops in the *remote* P1 reservoir that are widely separated in frequency from ^{13}C spins. In a simplistic picture, shown in Fig. 1C, relaxation originates from *pairs* of P1 centers in the same ^{14}N nuclear manifold (energy-mismatched by δ) undergoing spin flip-flop processes, and flipping a ^{13}C nuclear spin (when $\omega_L \approx \delta$) in order to make up the energy difference. In reality, the overall relaxation is constituted out of the several such processes over the entire P1 electronic spectrum.

Let us now assume the stochastic process $s_z(t)$ is Gaussian with zero mean and an autocorrelation function $g(\tau) = \exp(-\tau/\tau_c)$ with correlation time $\tau_c = 1/\langle d_{ee} \rangle$. The spectral density function $S(\omega) = \frac{1}{\sqrt{2\pi}} \int_{-\infty}^{\infty} g(\tau) e^{-i\omega\tau} d\tau$ that quantifies the power of the spin flipping noise components at various frequencies is then a Lorentzian, $S(\omega) = 2\tau_c/(1 + \omega^2\tau_c^2)$. Going further now into an interaction picture respect to $\omega_L I_z$, $\mathcal{H}_I^{(I)} =$

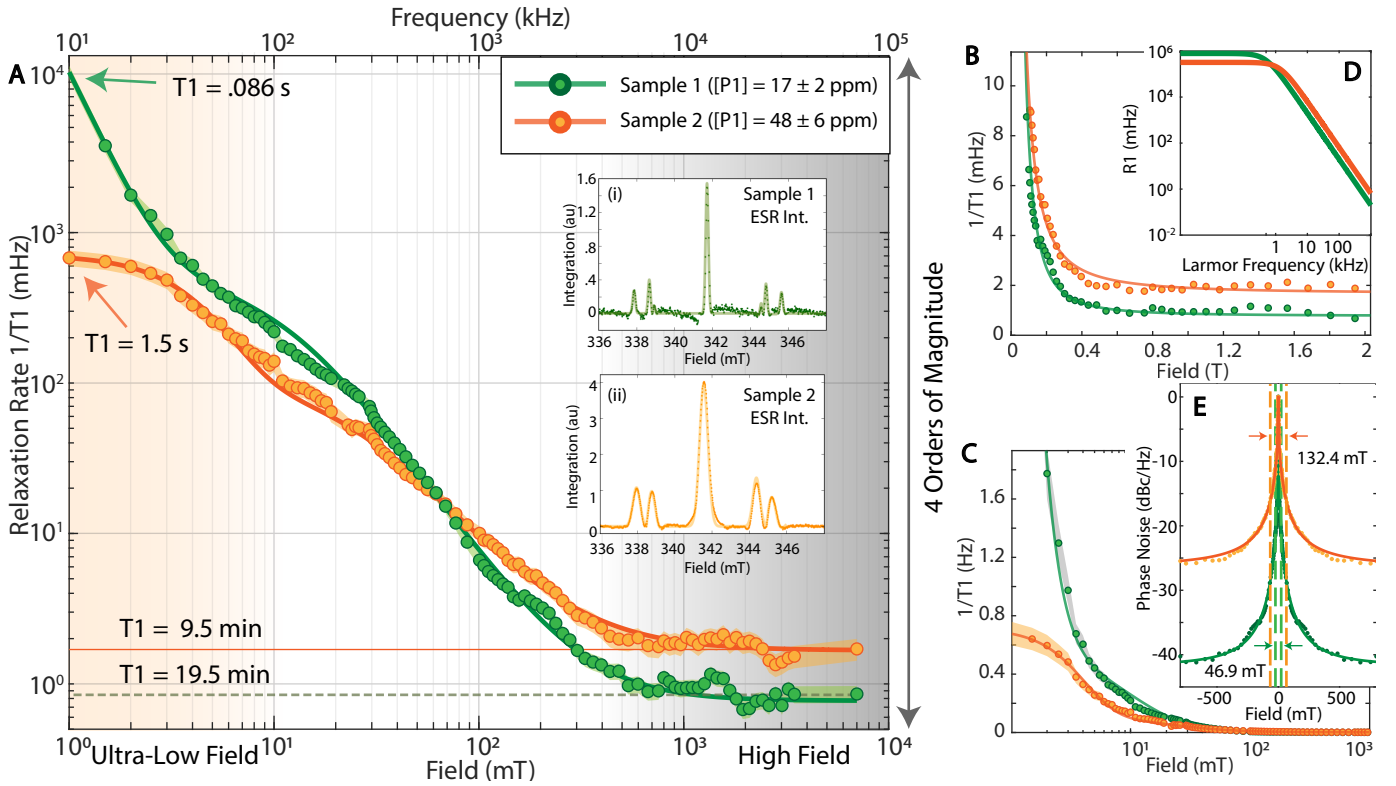


Figure 3. Hyperpolarized relaxometry at natural abundance ^{13}C relaxation rate over four decades of field 1 mT - 7 T (lower axis) for Samples 1 and 2, probing spin-flipping spectral density from 1 kHz to 75 MHz (upper axis). (A) *Relaxation rate* on a logarithmic scale, showing steep field dependence that spans four orders of magnitude in T_1 , falling to sub-second lifetimes at ultra-low fields below $B_K^{(2)}$, and saturating to lifetimes greater than 10 min. beyond $B_K^{(1)}$. Orange and green data correspond to CVD samples with different concentration of P1 centers [31] (legend). Solid lines are fits to a combination of two Tsallian functions. Shaded regions represent error bounds originating from our accelerated data collection strategy (see Supplemental Information [40]). *Insets*: X-band ESR spectra. (B) *High field behavior* shows saturating knee field $B_K^{(1)}$ occurs at higher field for Sample 2. (C) *Low field behavior*, where intriguingly Sample 2 with a higher P1 concentration has a lower relaxation rate. (D) *Calculated relaxation rate* $R_1(\omega_L)$ arising from the coupling of the ^{13}C spins with the interacting P1 reservoir for the case of 17 ppm (green) and 48 ppm (orange) electron concentrations, showing qualitative agreement with the experimental data from Samples 1 and 2. (E) *Comparing effective phase noise* $S_p(\omega)$ for the two samples on a semi-log scale. For clarity, data is mirrored on the X-axis and phase noise normalized against relaxation rates at $\omega_0=1$ mT. Solid lines are fits to Tsallian functions. Dashed vertical lines indicate the theoretical widths obtained from the the respective estimates of $2\langle d_{ee} \rangle$ and 131.89 mT, matching very closely the experiments.

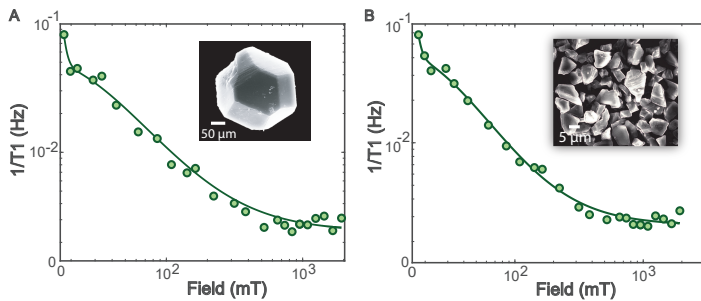


Figure 4. ^{13}C nuclear relaxation in microdiamond powder. Relaxation field maps for the randomly oriented natural abundance ^{13}C microdiamond powder Samples 3 and 4 of sizes (A) 200 μm and (B) 5 μm respectively with accompanying SEM images (insets). Data is obtained by measuring the full relaxation curve at every field point, and is qualitatively similar to the single crystal results in Fig. 3.

$\langle A_{zx} \rangle s_z(t) \left(e^{-i\omega_L I_z t'} I_x e^{i\omega_L I_z t'} \right)$. The survival probability of the spin is, $p(t) = \frac{1}{2} \text{Tr} \left\{ I_z e^{i\mathcal{H}_I^{(1)} t} I_z e^{-i\mathcal{H}_I^{(1)} t} \right\} \sim e^{-\chi(t)}$ where in an average Hamiltonian approximation, retaining effectively time-

independent terms, the effective relaxation rate $\chi(t) \approx R_1 t$ just can be obtained by *sampling* of the spectral density resonant with the nuclear Larmor frequency ω_L at each field point. This is the basis behind noise spectroscopy of the underlying T_1 process [49]. We recover then the familiar Bloembergen-Purcell-Pound (BPP) result [50, 51], where the relaxation rate,

$$\frac{1}{T_1^{(1)}} = R_1^{(1)}(\omega_L) = \langle A_{zx}^2 \rangle S(\omega_L) = \langle A_{zx}^2 \rangle \frac{\langle d_{ee} \rangle}{\omega_L^2 + \langle d_{ee} \rangle^2} \quad (3)$$

The inter-spin couplings can be estimated from the typical inter-spin distance $\langle r_e \rangle = (3/4\pi \ln 2)^{1/3} N_e^{-1/3}$, where $N_e = (4 \times 10^{-6} P_e) / a^3 [\text{m}^{-3}]$ is the electronic concentration in inverse volume units and $a = 0.35$ nm the lattice spacing in diamond [35]. The couplings are now related to the second moment of the electronic spectra [48] $M_{2e} = \frac{9}{20} (g\mu_B)^2 \frac{1}{\langle r_e \rangle^6}$, where $g \approx 2$ is the electron g-factor, and $\mu_B = 9.27 \times 10^{-21}$ erg/G the Bohr magneton in cgs units. This gives the Lorentzian estimate $\langle d_{ee} \rangle \approx \gamma_e \sqrt{\frac{8}{\pi} M_{2e}}$ [Hz] $\approx 10.5 P_e$ [mG], that scales approximately linearly with electron concentration P_e [35]. For Samples 1 and 2 with varied P_e we obtain spectral widths $\langle d_{ee} \rangle = 0.5$ kHz and 1.42 kHz respectively, corresponding to field-profile widths of 46.9 mT

and 132.4 mT respectively. These would correspond to inflection points $B_K^{(1)} = \frac{\langle d_{ee} \rangle}{2\gamma_n}$ in the relaxometry data at fields 23.5 mT and 66.2 mT respectively. These values are in remarkable and quantitative agreement with the experimental data (see also Fig. 3E). Moreover, we expect that these turning points (scaling $\propto P_e$) are *independent* of ^{13}C enrichment η , in agreement with the data in Fig. 2 (see also Fig. 5).

From lattice considerations (see [40]), we can also estimate the value of the effective hyperfine coupling $\langle A_{zx} \rangle$ in Eq. (3), which we expect to grow slowly with P_e . We make the assumption that there is barrier of $r_0 \approx 2.15$ nm around every P1 center in which the ^{13}C spins are “unobservable” because their hyperfine shifts exceed the measured ^{13}C linewidth $\Delta f_{\text{det}} \approx 2$ kHz. Our estimate can be accomplished by sitting on a P1 spin, and evaluating $\langle A_{zx} \rangle = [\langle A_{zx}^2 \rangle]^{1/2}$, where the second moment [48], $\langle A_{zx}^2 \rangle = \frac{1}{N} \left[\frac{\mu_0}{4\pi} \gamma_e \gamma_n \hbar \right]^2 \sum_j \frac{(3 \sin \vartheta_j \cos \vartheta_j)^2}{r_j^3}$ with N being the relative number of ^{13}C spins per P1 spin, and ϑ_j the angle between the P1- ^{13}C axis and the magnetic field, and index j runs over the region between neighboring P1 spins. This gives,

$$\langle A_{zx}^2 \rangle \approx \left(\frac{\mu_0}{4\pi} \gamma_e \gamma_n \hbar \right)^2 \frac{6}{5} \frac{1}{\langle r_e \rangle^3} \left(\frac{1}{r_0^3} - \frac{1}{\langle r_e \rangle^3} \right) \quad (4)$$

For the two samples, we have $\langle r_e \rangle = 4.8$ nm and 3.39 nm respectively, giving rise to the effective P1- ^{13}C hyperfine interaction $\langle A_{zx}^2 \rangle \approx 0.39$ [(kHz) 2] and $\langle A_{zx}^2 \rangle \approx 0.45$ [(kHz) 2] respectively. These values are also consistent with direct numerical estimates from simulated diamond lattices (see [40]). The simple model stemming from Eq. (2) and Eq. (3) therefore predicts that the effective hyperfine coupling $\langle A_{zx} \rangle$ increases slowly with the electron concentration P_e , with the electron spectral density width $\langle d_{ee} \rangle \propto P_e$.

Finally, from Eq. (3) we can estimate the zero-field rate stemming from this relaxation process, $R_1(0) = \frac{\langle A_{zx}^2 \rangle}{\langle d_{ee} \rangle} \approx 777$ [s $^{-1}$] and 317.5 [s $^{-1}$] respectively. Fig. 3D calculates the resulting relaxation rates from this process $R_1(\omega_L)$ in a logarithmic plot. It shows good semi-quantitative agreement with the data in Fig. 3A and captures the experimental observation that the rates of the two samples “cross over” at a particular field. It is instructive to represent the data in terms of effective “phase noise” (see Fig. 3E), denoted logarithmically as, $S_p(\omega_L) = 10 \log \left(\frac{R_1(\omega_0)}{R_1(\omega_L)} \right)$ [dBc/Hz], where $\omega_0 \rightarrow 0$ represents the relaxation rates approaching zero field. Fig. 3E shows this for the two samples, employing $\omega_0 = 1$ mT, and with the estimated field-linewidths displayed by the dashed lines. This makes evident that the high field spin-flipping noise seen by the ^{13}C nuclei is about 15 dB lower in Sample 1.

While Eq. (3) is the dominant relaxation mechanism operational at moderate fields, let us now turn our attention to the behavior at ultralow fields in Fig. 3. Eq. (2) provides the framework to consider the effect of *single* P1 and NV electrons to the relaxation of ^{13}C nuclei. In this case the stochastic process $s_z(t)$ arises not on account of inter-electron couplings, but due to individual T_{1e} processes operational on the electrons, due to for instance coupling to lattice phonons. The width of the spectral density is then given by T_{1e} ,

$$\frac{1}{T_1^{(2)}} = R_1^{(2)}(\omega_L) = \langle A_{zx}^2 \rangle \frac{T_{1e}}{1 + \omega_L^2 T_{1e}^2} \quad (5)$$

While T_{1e} is also field-dependent, and dominated by two-phonon

Raman processes at moderate-to-high field, typical values of $T_{1e} \sim 1$ ms [52], give rise to Lorentzian relaxometry widths of ≈ 1 kHz, corresponding to field turning points of $B_K^{(2)} \approx \frac{1}{2\gamma_n T_{1e}} = 0.1$ mT.

Let us finally comment on the role NV centers themselves as a source of ^{13}C relaxation. Since NV concentrations are low for samples under study (see Table I), with NV-NV coupling strengths $\lesssim 25$ kHz, relaxation processes stemming from pairs of NV centers have a negligible contribution in comparison to single NV driven processes. Moreover, close-shell ^{13}C nuclei that are most sensitive to this relaxation channel are unobservable in our experiments since they are hyperfine shifted by $\delta \approx \frac{A_{zx} \Delta \sin \vartheta}{\gamma_e B + \Delta \cos \vartheta}$ beyond the NMR detection band width ≈ 20 kHz, where ϑ is the angle of the N-V axis to the $B=7$ T detection field.

Effect of ^{13}C enrichment: – To systematically probe this low-field behavior as well as consider the effect of couplings within the ^{13}C reservoir, we consider in Fig. 5 diamond crystals with varying ^{13}C enrichment η and approximately identical NV and P1 concentrations (Samples 5-7). With increasing enrichment, a third relaxation mechanism becomes operational, wherein at low fields it becomes possible to dissipate Zeeman energy into the dipolar bath. The field dependence of this process is expected to be more Gaussian, centered at zero field and have a width $\sim \langle d_{CC} \rangle$ the mean inter-spin dipolar coupling between ^{13}C nuclei. We can estimate (see [40]) these couplings from the second moment, $\langle d_{CC} \rangle = \frac{1}{N} \sum_j \left[\sum_k \left(\frac{\mu_0}{4\pi} \hbar \gamma_n^2 (3 \cos^2 \vartheta_{jk} - 1) \right)^2 / r_{jk}^6 \right]^{1/2}$

where in a lattice of size ℓ , $N = N_C \ell^3$ refers to the number of ^{13}C spins, and the spin density $N_C = 0.92\eta$ spins/nm 3 . Here $\vartheta_{jk} = \cos^{-1} \left(\frac{\mathbf{r}_{jk} \cdot \mathbf{B}_{\text{relax}}}{r_{jk} B_{\text{relax}}} \right)$ is the angle between the inter-nuclear vector and the direction of the magnetic field. In the numerical simulations (outlined in [40]), we evaluate the case consistent with experiments wherein the single crystal samples placed flat, i.e. with $\mathbf{B}_{\text{relax}} \parallel [001]$ crystal axis. As a result, for ^{13}C spins on adjacent (nearest-neighbor) lattice sites, $\vartheta_{jk} = 54.7^\circ$ is the magic angle and $d_{jk}^{\text{CC}} = 0$.

We find $\langle d_{CC} \rangle \approx 850$ Hz for natural abundance samples and a scaling $\langle d_{CC} \rangle \propto \eta^{1/2}$ with increasing enrichment. This is in good agreement with the experimentally determined linewidths (see [40]). We thus expect a turning point at low fields, $B_K^{(2)} \sim \frac{\langle d_{CC} \rangle}{2\gamma_n}$, for instance ≈ 39 μT for natural abundance samples, but scaling to ≈ 0.46 mT in case of the 100% enriched Sample 7. In real experiments, it is difficult to distinguish between this process and that arising directly from single electrons in Eq. (5), and hence we assign the same label to this field turning point.

Performing hyperpolarized relaxometry (see Fig. 5) we observe that increasing enrichment leads to a fall in nuclear T_1 s, evident both at low (Fig. 5A) and high (Fig. 5B) fields. R_1 rates for the diamonds with ^{13}C concentrations of 10% and 100% (Samples 6 and 7) are obtained by taking the full relaxation decay curves at every field point, while for the 3% enriched diamond (Sample 5) we use an accelerated data collection strategy (see [40]) on account of the inherently long T_1 lifetimes. On a logarithmic scale (Fig. 5B), we observe the knee field $B_K^{(1)}$ is virtually identical across all the samples, indicating it is a feature independent of ^{13}C enrichment, originating from interactions with the electronic spin bath. This is in good agreement with the model in Eq. (3). A useful means to evaluate the inflection points from the zeros of the second derivative of the Tsallian fits, as indicated in the inset of Eq. (3)A. Moreover, the lower inflection field $B_K^{(2)}$ scales to higher fields with increasing enrichment η , pointing to its origin

from *internuclear* dipolar effects. At the low fields, we also notice that the samples with lower enrichment have higher relaxation rates, and with steeper field-profile slopes (Fig. 5B). This is once again consistent with the model that the spectral density height and width being probed scales with $\langle d_{CC} \rangle$.

Changes in the nuclear lifetimes are also reflected directly in the DNP polarization buildup curves, shown in Fig. 5C. We perform here hyperpolarization of all the samples under the same conditions, sweeping the entire $m_s=+1$ manifold at $B_{\text{pol}}=36$ mT, sweeping over the full NV ESR spectrum. We notice that polarization buildup is predominantly mono-exponential (dashed lines in Fig. 5C), except for at natural abundance ^{13}C , where a bi-exponential growth (solid line) is indicative of nuclear spin diffusion. Data demonstrates that highly enriched samples have progressively smaller polarization buildup times (see Fig. 5E) on account of limited nuclear lifetimes at B_{pol} .

Moreover, the experimental data allows us to quantify the “homogenization” of polarization in the lattice. We assign a spin diffusion coefficient $D = \frac{\langle r_n \rangle^2}{30T_{2n}}$ (see Fig. 5F) where the T_{2n} are evaluated here by only taking the dipolar contribution to the linewidth, $T_{2n} \approx 1/\langle d_{CC} \rangle$ [53]. Given a total time bounded by T_1 , we can calculate the rms overall diffusion length [54] as $\sigma = \sqrt{2DT_1}$ that is displayed as the blue points in Fig. 5F. Also for reference is plotted the mean NV-NV distance ≈ 12 nm at 1 ppm concentration (dashed region in Fig. 5F), indicating that to a good approximation that the optically pumped polarization reaches to all parts of the diamond lattice between the NV centers.

We comment finally that determining the origins of ^{13}C relaxation in enriched samples can have several technological applications. Enrichment provides an immediate means to realize quantum registers and sensing modalities constructed out of hybrid NV- ^{13}C spin clusters, and as such ascertaining nuclear relaxation profiles is of practical importance for such applications. Low η ($\leq 3\%$) naturally engender NV- ^{13}C pairs that can form quantum registers [55–57]. The nuclear spin can serve as an ancillary quantum memory that, when employed in magnetometry applications, can provide significant boosts in sensing resolution [19, 58]. With increasing ^{13}C concentrations $\eta \gtrsim 10\%$ a single NV center can be coupled to several ^{13}C nuclei forming natural nodes for a quantum information processor, and where the nuclear spins can be actuated directly by hyperfine couplings to the NV electron [59, 60]. Approaching full enrichment levels ($\eta = 100\%$), internuclear couplings become significant, permitting hybridized nuclear spin states and decoherence protected subspaces [61] for information storage. In bulk quantum sensing too, for instance applied to diamond based gyroscopes [18, 62], the high density of ^{13}C sensor spins ($\sim 10^{22}/\text{cm}^3$), as much as $> 10^5$ times the number of NV centers, can be harnessed to increase sensitivity.

Discussion: – Experimental results in Fig. 3 and Fig. 5 substantiate the ^{13}C relaxation pathways operational at different field regimes, and potentially highlight the particularly important role played by the electronic reservoir towards setting the spin lifetimes. To independently affirm this connection, we perform in Fig. 6 relaxometry under blue ($\lesssim 495$ nm) wavelengths where the P1 electrons ionize strongly. In these experiments, we operate at the relatively low excitation powers ~ 240 mW/mm² due to technical limitations related to sample heating. We observe a comparative *decrease* in nuclear T_1 with respect to decay in the dark (see Fig. 6). In contrast, we do not observe significant change in the lifetimes under 520 nm excitation. We believe that we are accessing an intermediate regime where the P1 ionization rate is slower than the interelectron flip-flop rate by $\langle d_{ee} \rangle$. As a result,

ionization is not rapid enough to decouple each spin flip-flop event between neighboring P1 centers. On the contrary, upon ionization and subsequent recapture, the P1 electrons can now cause spin relaxation over a lattice length scale that is longer than purely given by dipole-dipole interactions. This “stirring” of the electronic spin bath through blue irradiation, results in increased spectral density component at the nuclear Larmor frequency and consequently an increased relaxation rate.

Our experimental observations open the door to a number of intriguing future directions. First, they suggest the prospect of increasing nuclear lifetimes by raising the NV center conversion efficiency [63]. More generally, they point to the efficacy of materials science approaches towards reducing paramagnetic impurities in the lattice. Finally, it opens the possibility of employing coherent quantum control for dissipation engineering, to manipulate the spectral density profile seen by the nuclei and consequently lengthen their T_1 . Applying a “pulse sequence to increase T_1 ” has been a longstanding goal in magnetic resonance [64, 65], but is typically intractable because of inability to coherently control broad-spectrum phonon interactions. Instead here since the nuclear T_1 stems from electronic T_{2e} processes, these can be “echoed out”; In particular, the application of electron decoupling (such as WAHUA [66] or Lee-Goldburg [67] decoupling) on the P1 spin bath would suppress the inter-electron flip-flops, narrow the noise spectral density, and consequently shift the knee field $B_K^{(1)}$ to lower fields. Such T_1 gains just by spin driving at room temperature and without the need for cryogenic cooling, and consequent boosts in the hyperpolarization enhancements – scaling by the decoupling factor – will have far-reaching implications for the optical DNP of liquids under ambient conditions. Given the multi-frequency microwave control driving each of the ^{14}N manifolds would entail [68], an attractive alternate *all-optical* means is via the optical ionization of P1 centers faster than their flip-flop rate. The exact interplay between optical ionization and recapture rates required for T_1 suppression will be the subject of future work.

Conclusions: – Employing hyperpolarized relaxometry, we have mapped the ^{13}C nuclear spin lifetimes in a prototypical diamond quantum system over a wide field range, in natural abundance and enriched ^{13}C samples, and for both single crystals as well as powders. We observe a dramatic and intriguing field dependence, where spin lifetimes fall rapidly below a knee field of ~ 100 mT. The results indicate that the spin lifetimes predominantly arise from nuclear flip processes mediated by the P1 center electronic spin bath, and immediately opens the compelling possibility of boosting nuclear lifetimes by quantum control or optically induced electronic ionization. This has significant implications in quantum sensing, in building longer lived quantum memories, and in practically enhancing the ^{13}C hyperpolarization efficiency in diamond, with applications to hyperpolarized imaging of surface functionalized nanodiamonds and for the DNP of liquids brought in contact with high surface area diamond particles.

Acknowledgments: – We gratefully acknowledge discussions with A. Redfield, D. Sakellariou and J.P. King, and technical contributions from M. Gierth, T. McNelly, and T. Virtanen. C.A.M. acknowledges support from NSF through NSF-1401632 and NSF-1619896, from Research Corporation for Science Advancement through a FRED award, and research infrastructure from NSF Centers of Research Excellence in Science and Technology Center for Interface Design and Engineered Assembly of Low-Dimensional Systems (NSF-HRD-1547830).

Materials – Table I summarizes the particulars of the samples we employ in this study. ^{13}C enriched diamonds (Samples 5-7) used to conduct experiments in Fig. 2 and Fig. 5 were grown through chemical vapor deposition using a ^{13}C enrichment mixture of methane and nitrogen (660ppm, Applied Diamond Inc) as precursor followed by ^{13}C enrichments of 10%, 25%, 50%, and 100% to produce the respective percent-enriched diamonds [32]. To produce a NV-concentration of 1-10 ppm, the enriched samples were irradiated with 1 MeV electrons at a fluence of 10^{18} cm^{-2}

(Prism Gem LLC) then annealed for 2 hours at 800C. The natural abundance samples used in Fig. 3 (Samples 1-2) were grown under synthetic high pressure, high temperature conditions (Element 6, Sumitomo) [31] then annealed for 1 hour at 850°C. The NV and P1 concentration were measured to be 1.4 ± 0.02 ppm and 17 ± 2 ppm for the first sample and 6.9 ± 0.8 ppm and 48 ± 6 ppm for the second sample, respectively. The microdiamond powders in Fig. 4 (Samples 3-4), produced by HPHT techniques, were acquired from Element6 and Columbus Nanoworks respectively.

-
- [1] J. Preskill, *Proceedings of the Royal Society of London. Series A: Mathematical, Physical and Engineering Sciences* **454**, 385 (1998).
- [2] W. H. Zurek, *Reviews of modern physics* **75**, 715 (2003).
- [3] C. W. Gardiner and P. Zoller, *Quantum Noise: A Handbook of Markovian and Non-Markovian Quantum Stochastic Methods with Applications to Quantum Optics*, 3rd ed. (Springer-Verlag, 2004).
- [4] G. A. Álvarez and D. Suter, *Phys. Rev. Lett.* **107**, 230501 (2011).
- [5] D. Suter and G. A. Álvarez, *Reviews of Modern Physics* **88**, 041001 (2016).
- [6] L. Viola, E. Knill, and S. Lloyd, *Phys. Rev. Lett.* **85**, 3520 (2000).
- [7] L. Cywinski, R. M. Lutchyn, C. P. Nave, and S. DasSarma, *Phys. Rev. B* **77**, 174509 (2008).
- [8] M. J. Biercuk, H. Uys, A. P. VanDevender, N. Shiga, W. M. Itano, and J. J. Bollinger, *Nature* **458**, 996 (2009).
- [9] J. Bylander, S. Gustavsson, F. Yan, F. Yoshihara, K. Harrabi, G. Fitch, D. G. Cory, and W. D. Oliver, *Nature Physics* **7**, 5652570 (2011).
- [10] A. Ajoy, G. A. Álvarez, and D. Suter, *Phys. Rev. A* **83**, 032303 (2011).
- [11] C. A. Ryan, J. S. Hodges, and D. G. Cory, *Phys. Rev. Lett.* **105**, 200402 (2010).
- [12] S. Gustavsson, J. Bylander, F. Yan, P. Forn-Diaz, V. Bolkhovskiy, D. Braje, G. Fitch, K. Harrabi, D. Lennon, J. Miloshi, P. Murphy, R. Slattery, S. Spector, B. Turek, T. Weir, P. B. Welander, F. Yoshihara, D. G. Cory, Y. Nakamura, T. P. Orlando, and W. D. Oliver, *Phys. Rev. Lett.* **108**, 170503 (2012).
- [13] N. Bar-Gill, L. Pham, C. Belthangady, D. Le Sage, P. Cappellaro, J. Maze, M. Lukin, A. Yacoby, and R. Walsworth, *Nat. Commun.* **3**, 858 (2012).
- [14] J. Labaziewicz, Y. Ge, D. R. Leibbrandt, S. X. Wang, R. Shewmon, and I. L. Chuang, *Physical review letters* **101**, 180602 (2008).
- [15] F. Jelezko and J. Wrachtrup, *Physica Status Solidi (A)* **203**, 3207 (2006).
- [16] C. L. Degen, F. Reinhard, and P. Cappellaro, *Reviews of modern physics* **89**, 035002 (2017).
- [17] T. H. Taminiau, J. J. T. Wagenaar, T. van der Sar, F. Jelezko, V. V. Dobrovitski, and R. Hanson, *Phys. Rev. Lett.* **109**, 137602 (2012).
- [18] A. Ajoy and P. Cappellaro, *Phys. Rev. A* **86**, 062104 (2012).
- [19] T. Roskopf, J. Zopes, J. M. Boss, and C. L. Degen, *npj Quantum Information* **3**, 33 (2017).
- [20] J. J. L. Morton, A. M. Tyryshkin, R. M. Brown, S. Shankar, B. W. Lovett, A. Ardavan, T. Schenkel, E. E. Haller, J. W. Ager, and S. A. Lyon, *Nature* **455**, 1085 (2008).
- [21] D. J. Christle, A. L. Falk, P. Andrich, P. V. Klimov, J. U. Hassan, N. T. Son, E. Janzén, T. Ohshima, and D. D. Awschalom, *Nature Materials* **14** (2015).
- [22] P. V. Klimov, A. L. Falk, D. J. Christle, V. V. Dobrovitski, and D. D. Awschalom, *Science advances* **1**, e1501015 (2015).
- [23] J. Cai, A. Retzker, F. Jelezko, and M. B. Plenio, *Nature Physics* **9**, 168 (2013).
- [24] I. Lovchinsky, J. Sanchez-Yamagishi, E. Urbach, S. Choi, S. Fang, T. Andersen, K. Watanabe, T. Taniguchi, A. Bylinskii, E. Kaxiras, *et al.*, *Science* **355**, 503 (2017).
- [25] A. Ajoy, U. Bissbort, D. Poletti, and P. Cappellaro, *Physical Review Letters* **122**, 013205 (2019).
- [26] M. Cassidy, C. Ramanathan, D. Cory, J. Ager, and C. M. Marcus, *Physical Review B* **87**, 161306 (2013).
- [27] Y. Wu, F. Jelezko, M. B. Plenio, and T. Weil, *Angewandte Chemie International Edition* **55**, 6586 (2016).
- [28] A. Ajoy, K. Liu, R. Nazaryan, X. Lv, P. R. Zangara, B. Safvati, G. Wang, D. Arnold, G. Li, A. Lin, *et al.*, *Sci. Adv.* **4**, eaar5492 (2018).
- [29] A. Ajoy, X. Lv, E. Druga, K. Liu, B. Safvati, A. Morabe, M. Fenton, R. Nazaryan, S. Patel, T. F. Sjolander, J. A. Reimer, D. Sakellariou, C. A. Meriles, and A. Pines, *Review of Scientific Instruments* **90**, 013112 (2019), <https://doi.org/10.1063/1.5064685>.
- [30] Video showing working of wide dynamic range field cycler, <https://www.youtube.com/watch?v=rFlg5TDP9WY&feature=youtu.be>.
- [31] E. Scott, M. Drake, and J. A. Reimer, *Journal of Magnetic Resonance* **264**, 154 (2016).
- [32] A. J. Parker, K. Jeong, C. E. Avalos, B. J. Hausmann, C. C. Vasiliou, A. Pines, and J. P. King, *arXiv preprint arXiv:1708.00561* (2017).
- [33] A. Ajoy, R. Nazaryan, K. Liu, X. Lv, B. Safvati, G. Wang, E. Druga, J. Reimer, D. Suter, C. Ramanathan, *et al.*, *Proceedings of the National Academy of Sciences* **115**, 10576 (2018).
- [34] P. R. Zangara, S. Dhomkar, A. Ajoy, K. Liu, R. Nazaryan, D. Pagliero, D. Suter, J. A. Reimer, A. Pines, and C. A. Meriles, *Proceedings of the National Academy of Sciences*, 201811994 (2019).
- [35] E. Reynhardt, *Concepts in Magnetic Resonance Part A* **19A**, 20 (2003).
- [36] M. Lee, M. Cassidy, C. Ramanathan, and C. Marcus, *Physical Review B* **84**, 035304 (2011).
- [37] D. E. Waddington, M. Sarracanie, H. Zhang, N. Salameh, D. R. Glenn, E. Rej, T. Gaebel, T. Boele, R. L. Walsworth, D. J. Reilly, *et al.*, *Nature communications* **8**, 15118 (2017).
- [38] A. Ajoy, R. Nazaryan, E. Druga, K. Liu, A. Aguilar, B. Han, M. Gierth, J. T. Oon, B. Safvati, R. Tsang, *et al.*, *arXiv preprint arXiv:1811.10218* (2018).
- [39] Video showing ultraportable nanodiamond hyperpolarizer, <https://www.youtube.com/watch?v=IjnMh-sROK4>.
- [40] See supplementary online material.
- [41] C. Tsallis, S. V. Levy, A. M. Souza, and R. Maynard, *Physical Review Letters* **75**, 3589 (1995).
- [42] D. F. Howarth, J. A. Weil, and Z. Zimpel, *Journal of Magnetic Resonance* **161**, 215 (2003).
- [43] E. Rej, T. Gaebel, T. Boele, D. E. Waddington, and D. J. Reilly, *Nature communications* **6** (2015).
- [44] J. Isoya, H. Kanda, Y. Uchida, S. Lawson, S. Yamasaki, H. Itoh, and Y. Morita, *Physical Review B* **45**, 1436 (1992).
- [45] L. Dei Cas, S. Zeldin, N. Nunn, M. Torelli, A. I. Shames, A. M. Zaitsev, and O. Shenderova, *Advanced Functional Materials*, 1808362 (2019).
- [46] M. E. Drake, *Characterizing and Modeling Spin Polarization from Optically Pumped Nitrogen-Vacancy Centers in Diamond at High Magnetic Fields* (University of California, Berkeley, 2016).
- [47] E. Reynhardt and C. Terblanche, *Chemical physics letters* **269**, 464 (1997).

- [48] A. Abragam, *Principles of Nuclear Magnetism* (Oxford Univ. Press, 1961).
- [49] R. Kimmich and E. Anoardo, *Progress in nuclear magnetic resonance spectroscopy* **44**, 257 (2004).
- [50] N. Bloembergen, E. M. Purcell, and P. V. Pound, *Phys. Rev.* **73**, 679 (1948).
- [51] A. G. Redfield, *IBM Journal of Research and Development* **1**, 19 (1957).
- [52] A. Jarmola, V. Acosta, K. Jensen, S. Chemerisov, and D. Budker, *Physical review letters* **108**, 197601 (2012).
- [53] H. Hayashi, K. M. Itoh, and L. S. Vlasenko, *Physical Review B* **78**, 153201 (2008).
- [54] W. Zhang and D. G. Cory, *Phys. Rev. Lett.* **80**, 1324 (1998).
- [55] M. V. G. Dutt, L. Childress, L. Jiang, E. Togan, J. Maze, F. Jelezko, A. S. Zibrov, P. R. Hemmer, and M. D. Lukin, *Science* **316**, 1312 (2007).
- [56] P. Neumann, R. Kolesov, B. Naydenov, J. Beck, F. Rempp, M. Steiner, V. Jacques, G. Balasubramanian, M. L. Markham, D. J. Twitchen, S. Pezzagna, J. Meijer, J. Twamley, F. Jelezko, and J. Wrachtrup, *Nat Phys* **6**, 249 (2010).
- [57] A. Reiserer, N. Kalb, M. S. Blok, K. J. van Bemmelen, T. H. Taminiau, R. Hanson, D. J. Twitchen, and M. Markham, *Physical Review X* **6**, 021040 (2016).
- [58] A. Laraoui, F. Dolde, C. Burk, F. Reinhard, J. Wrachtrup, and C. A. Meriles, *Nature communications* **4**, 1651 (2013).
- [59] N. Khaneja, *Phys. Rev. A* **76**, 032326 (2007).
- [60] T. W. Borneman, C. E. Granade, and D. G. Cory, *Phys. Rev. Lett.* **108**, 140502 (2012).
- [61] N. Kalb, A. A. Reiserer, P. C. Humphreys, J. J. Bakermans, S. J. Kamerling, N. H. Nickerson, S. C. Benjamin, D. J. Twitchen, M. Markham, and R. Hanson, *Science* **356**, 928 (2017).
- [62] D. Maclaurin, M. W. Doherty, L. C. L. Hollenberg, and A. M. Martin, *Phys. Rev. Lett.* **108**, 240403 (2012).
- [63] D. Farfurnik, N. Alfasi, S. Masis, Y. Kauffmann, E. Farchi, Y. Romach, Y. Hovav, E. Buks, and N. Bar-Gill, *Applied Physics Letters* **111**, 123101 (2017).
- [64] M. Carravetta, O. G. Johannessen, and M. H. Levitt, *Physical review letters* **92**, 153003 (2004).
- [65] G. Pileio, M. Carravetta, and M. H. Levitt, *Proceedings of the National Academy of Sciences* **107**, 17135 (2010).
- [66] J. Waugh, L. Huber, and U. Haeberlen, *Phys. Rev. Lett.* **20**, 180 (1968).
- [67] M. Lee and W. Goldburg, *Phys. Rev. A* **140**, 1261 (1965).
- [68] E. Bauch, C. A. Hart, J. M. Schloss, M. J. Turner, J. F. Barry, P. Kehayias, and R. L. Walsworth, *arXiv preprint arXiv:1801.03793* (2018).
- [69] Video showing method of "printing" coils for inductive spin readout, <https://www.youtube.com/watch?v=7oP7KERSoNM/>.

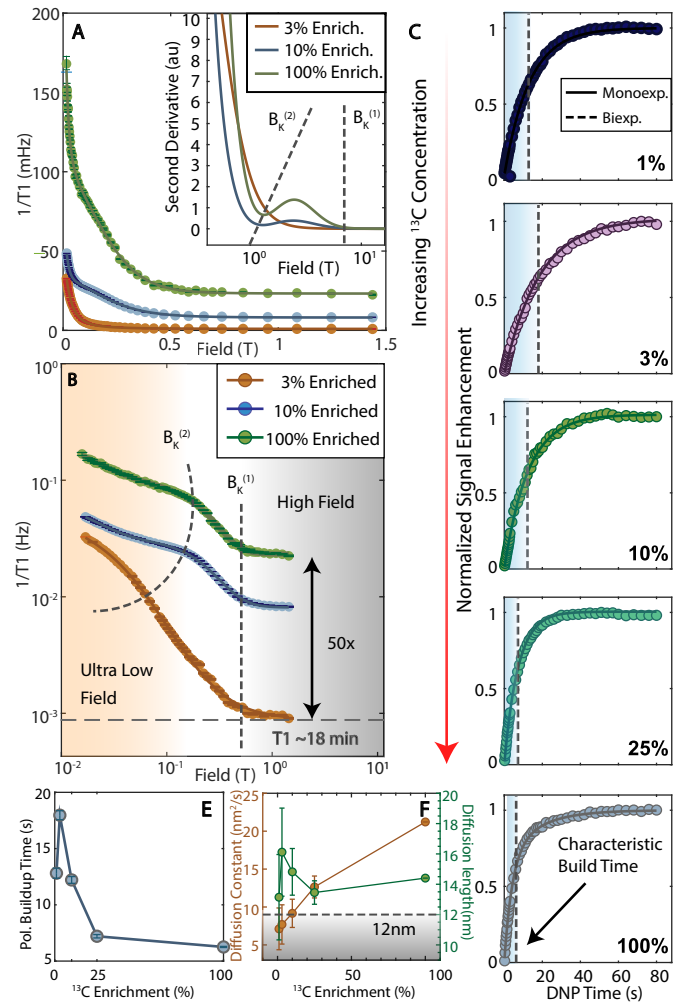


Figure 5. **Variation with ^{13}C enrichment.** Experiments are performed on single crystal samples placed so that all the NV center orientations are identical at 54.7° to $B_{\text{pol}}=36$ mT. (A) *Relaxation rates* on linear and (B) logarithmic field scale for Samples 5 through 7 with ^{13}C concentrations of 3%, 10%, and 100%, making evident an increase in relaxation rate with increasing ^{13}C enrichment at low and high fields. Solid lines are Tsallian fit. Error bars are obtained from the relaxation data at various fields. Characteristic knee field $B_K^{(1)}$ (dashed vertical line) at moderate fields is independent of enrichment, evident in the inset. Knee field at ultra-low fields $B_K^{(2)}$ qualitatively is indicated by the dashed line that serves as a guide to the eye. *Inset*: Second derivative of the fitted lines, showing the knee fields at the zero-crossings. (C) *DNP polarization buildup curves* also reflect differences in the nuclear spin lifetimes, displaying saturation at much shorter times upon increasing enrichment. DNP in all curves are performed at 36 mT sweeping the entire $m_s = +1$ manifold. (D) Polarization buildup times extracted from the data showing that faster nuclear spin relaxation limits the final obtained hyperpolarization enhancements in highly enriched samples. (E) *Spin diffusion constant and diffusion length* for ^{13}C nuclei numerically estimated from the data as a function of lattice enrichment. Dashed line indicates the mean inter-electron distance $\langle r_{\text{NV}} \rangle \approx 12$ nm between NV centers at 1 ppm concentration, indicating that spin diffusion can homogeneously spread polarization in the lattice almost independent of ^{13}C enrichment.

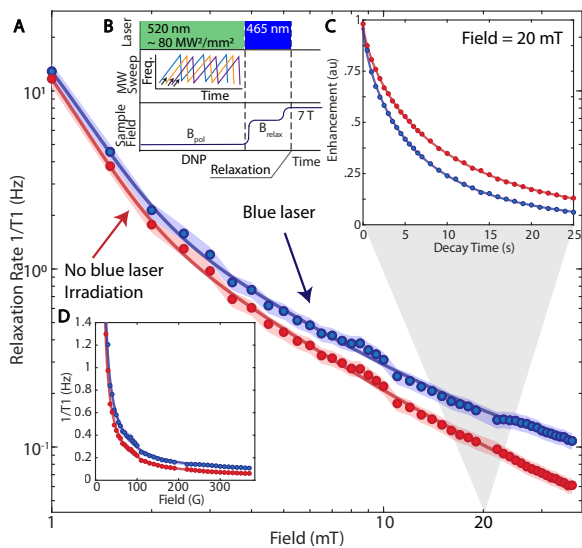


Figure 6. **Dynamic optical engineering of electron spin density.** Panel A denotes ^{13}C relaxation rate on a logarithmic scale for Sample 1 employed in Fig. 3 with relaxation dark (red points) and under low power (80 mW/mm^2) blue (465 nm) irradiation (blue points). Shaded regions represent error bounds (see [40]). (B) Schematic time sequence of the experiment. (C) Exemplary decay curves obtained at 20 mT . (D) Relaxation rates on linear field scale. We observe that the blue radiation leads to a decrease in ^{13}C nuclear lifetimes, which we hypothesize arises from fluctuations introduced in the electronic spin bath upon recapture after P1 center ionization. This illustrates that the electronic spin spectral density can be optically manipulated, and potentially ultimately also narrowed under sufficiently high-power ionization irradiation.

Supplementary Information

Hyperpolarized relaxometry based nuclear T_1 noise spectroscopy in hybrid diamond quantum registers

A. Ajoy,¹ B. Safvati,¹ R. Nazaryan,¹ J. T. Oon,¹ B. Han,¹ P. Raghavan,¹ R. Nirodi,¹ A. Aguilar,¹ K. Liu,¹
X. Cai,¹ X. Lv,¹ E. Druga,¹ C. Ramanathan,² J. A. Reimer,³ C. A. Meriles,⁴ D. Suter,⁵ and A. Pines¹

¹ Department of Chemistry, University of California Berkeley, and Materials Science Division Lawrence Berkeley National Laboratory, Berkeley, California 94720, USA. ² Department of Physics and Astronomy, Dartmouth College, Hanover, New Hampshire 03755, USA. ³ Department of Chemical and Biomolecular Engineering, and Materials Science Division Lawrence Berkeley National Laboratory University of California, Berkeley, California 94720, USA. ⁴ Department of Physics, and CUNY-Graduate Center, CUNY-City College of New York, New York, NY 10031, USA. ⁵ Fakultät Physik, Technische Universität Dortmund, D-44221 Dortmund, Germany.

CONTENTS

References	8
I. EPR Measurements in Fig. 3	11
II. Field Cycling	11
III. Data Processing	12
A. Fit models	12
B. Accelerated data collection strategy	13
C. Error estimates	14
IV. Model For Hyperpolarized Relaxometry	14
A. Lattice estimates for electron reservoir	14
B. Lattice estimates for ^{13}C reservoir	15
C. Lattice estimates for hyperfine couplings to NV and P1 reservoirs	17

I. EPR MEASUREMENTS IN FIG. 3

EPR spectra of Samples 1 and 2 in Fig. 3 were examined with a microwave power 6 mW, averaging over 50 sweeps, with modulation amplitudes of 0.1 mT and 0.01 mT and at sweep fields of 3350 - 3500 G and 3300 - 3600 G for the two samples respectively. Concentrations of P1 centers were estimated by using a CuSO_4 reference outlined in Ref. [31].

In order to determine the linewidths of the EPR spectra, a script was written to determine the data range at which Tsallis fits should be applied by first finding the indices where the spectral maxima and minima occurred. Midpoints were then determined between the maximum and minimum indices and the first derivative of the Tsallis function was fit to the ranges between the calculated midpoints. Because the baseline was not perfectly zeroed, jumps in the fit values occurred between each range. Applying fits to each individual peak rather than applying one Tsallis function to multiple peaks produced a better baseline correction since the offsets differed between ranges. Each peak was corrected by subtracting the median y-value over the fit range and then making manual corrections if necessary. Once the corrections were completed, the first integrals over each individual range were obtained using trapezoidal integration. The resulting integral arrays were then concatenated and a second integral was obtained. The resulting first integral allowed us to find the line widths of each P1 peak (FWHMs), and the second integral resembled a step function from which the relative step heights of each P1 peak could be found. To account for the hyperfine splittings of the P1 spectra an average over all peaks linewidths was taken and weighted by the height of each peak. The ratio of the averaged linewidths between the two samples in Fig. 3 was found to be 2.97, consistent with the ratio

of the P1 concentration of the two samples up to the accuracy of the concentration estimates.

II. FIELD CYCLING

T_1 noise spectroscopy relies on our ability to rapidly vary the magnetic field experienced by a test sample using a homemade shuttling system built over a 7 T superconducting magnet [29]. Samples are held in an NMR tube (Wilman 8 mm OD, 1 mm thickness) (see Fig. S1D) and pressure-fastened from below the magnet onto a lightweight, carbon fiber shuttling rod (Rock West composites). Using a high precision (50 μm) conveyor actuator stage (Parker HMRB08) (see Fig. S1B), we are able to repeatedly and consistently shuttle from low fields (~ 30 mT) below the magnet for polarization to high fields (7 T) within the magnet for NMR detection at sub-second speeds (< 700 ms). The instrument is interfaced with a low-cost hyperpolarizer (See [38] for details), allowing generation and detection of bulk nuclear polarization. Because the average shuttling time is small compared to the nuclear T_1 lifetimes (see Fig. S2) – particularly at fields above 100 mT – our resulting NMR signals are recorded with minimal loss in enhancement. High precision shuttling allowed for the measurement of a full z-direction field map (see Fig. S3), where the field was measured as a function of position using an axial Hall probe for fields less than 3.5 T. To accommodate the fast shuttling technique, the conventional NMR probe was modified to be hollow, allowing for shuttling through the probe to low magnetic fields below the magnet. Custom made “printed” coils (see [69]) are employed for direct inductive detection of the NMR signals [29].

From the field map in Fig. S3 it is clear that the gradient experienced by the samples is field-dependent. To quantify the field inhomogeneity during the signal decay process, we numerically estimate the gradient at each height from the acquired field map. The largest gradient occurs when the sample is just entering the bore of the magnet, where the field is around 2 T and the gradient is ~ 26 mT/mm. Because our samples normally occupy a height under 0.5 mm within the sample tube, they will experience a maximum field variation of about 13 mT within the sample. Yet because at this height the magnetic field is so large, this gradient only adds a 0.5% field variation throughout the lattice and so this effect can be ignored. For heights closer to the knee fields that we study ~ 100 mT, the field gradient is on the order of 1 mT/mm and so the gradient can be similarly ignored.

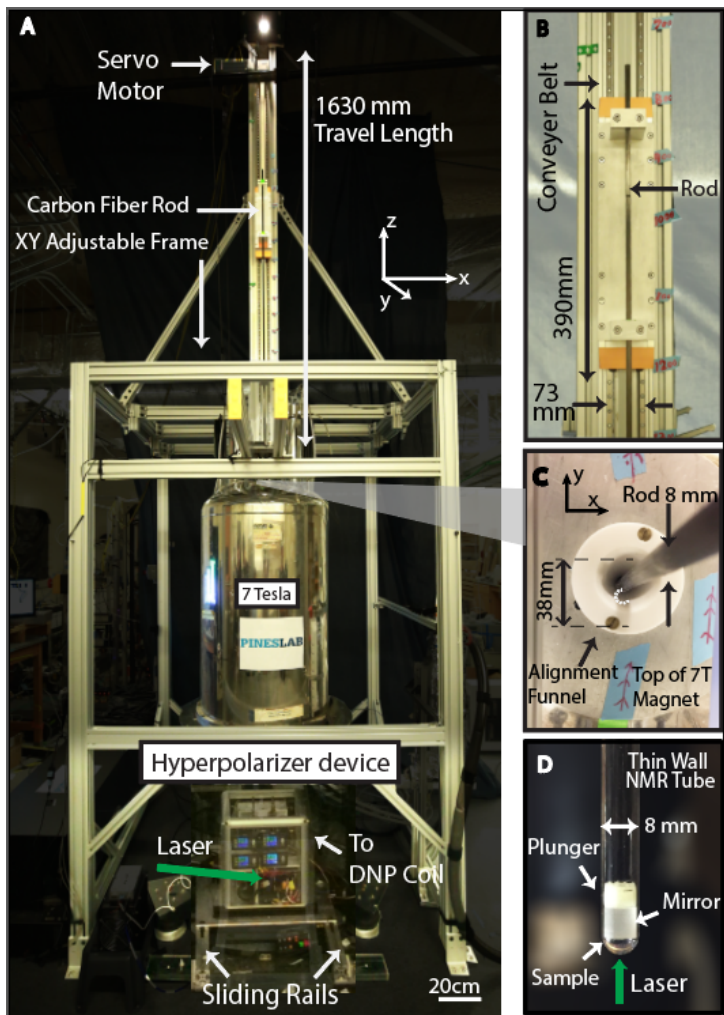


Figure S1. **Field cycling device** interfaced with portable diamond hyperpolarizer. (A) Mechanical shuttler is connected to a 7 T magnet and interfaced to a portable hyperpolarizer. Sliding rails attached to the bottom of the device allow for adjustment of hyperpolarizer box and centering of sample above coil. (B) The carbon-fiber shuttling rod is moved along a conveyor belt through use of a twin-carriage actuator. (C) The 8 mm shuttling rod is centered in the 38 mm magnet bore, with a Teflon guide for self-alignment. (D) Diamond sample is held within an 8mm wide NMR tube, and fitted with a plunger and mirror to prevent excess movement of sample and bolster efficacy of optical pumping.

III. DATA PROCESSING

A. Fit models

Nuclear T_1 at a given magnetic field is determined by measuring the decay of NMR signal $\varepsilon(t)$ with respect to time t spent decaying at that field. By measuring the change in signal over various times, relaxation decay curves are determined, and $T_1(B)$ estimated. We find that all the data can be fit to a stretched exponential of the form (see Fig. S4A),

$$\varepsilon(t) = \varepsilon_0 e^{-\left(\frac{t}{T_1(B)}\right)^p}, \quad (6)$$

where $p \in (0, 1]$ is a stretch factor [52], and ε_0 represents the bare signal enhancement obtained from DNP and assuming no loss during shuttling. For certain samples, such as the 10% ^{13}C sample in Fig. 2C, we observe that $p \approx 1$, while for most samples with low ^{13}C enrichment (including at natural abundance), $p \in (0.5, 1)$.

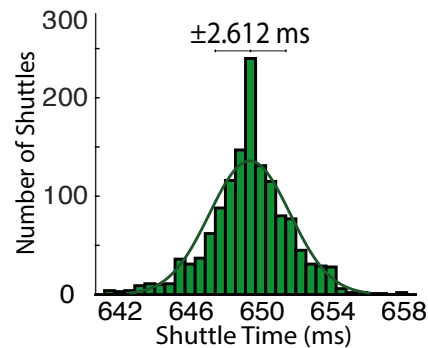


Figure S2. **Sample shuttling repeatability.** Shuttler operation (1400 runs) between polarization (~ 30 mT) and detection (7 T) locations, distance of approximately 928 mm depending on sample holder inserted. Samples are pressure held onto hollow carbon fiber rod along the center of the magnet bore and shuttled using a mechanical actuator activated by synchronized pulse trigger. This demonstrates high stability for repeated experiments, with average travel times of 648 ± 0.6 ms.

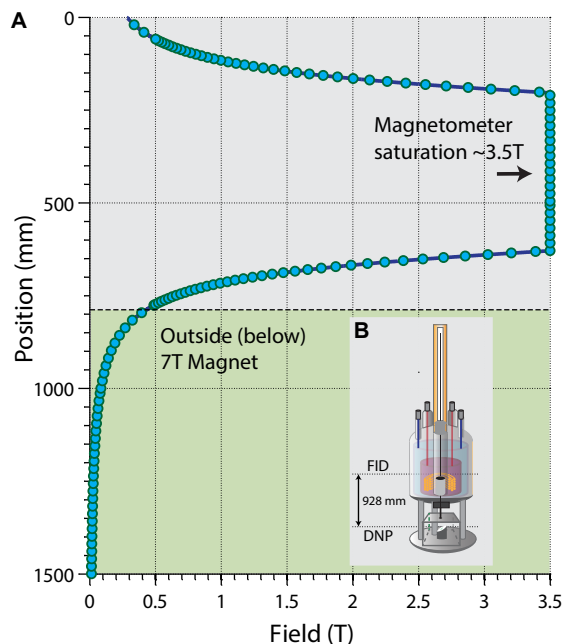


Figure S3. **Field map** (A) Measurement of longitudinal (z axis) magnetic field over full field cycler range using a sensitive magnetometer. Data points were attained by shuttling magnetic field probe through center of the magnetic bore while held within the hollow carbon fiber shuttling rod, limiting accuracy to the $50 \mu\text{m}$ precision of the actuator. Position of magnet entrance is shown to demonstrate fringe field profile. Due to magnetometer constraints, high field measurements saturate at 3.5 T. (B) Polarization is generated ~ 928 mm from the NMR coil, depending on the sample holder. This range can be traveled in sub-second speeds (see Fig. S1), allowing fast transport of hyperpolarized diamonds from low fields below to center of magnet with minimal relaxation loss.

We ascribe this stretch factor to be arising from spin diffusion of the inhomogeneous polarization in the lattice that is driven by the DNP process.

By measuring the relaxation rate $R_1(B) = 1/T_1(B)$ over a range of magnetic fields allowed by the field cycler, a relaxation field map $R_1(B)$ can be obtained, as shown in Fig. 2B. These relaxation profiles are then fit to a sum of two Tsallis distributions [36], a generalization of Gaussian and Lorentzian functions that

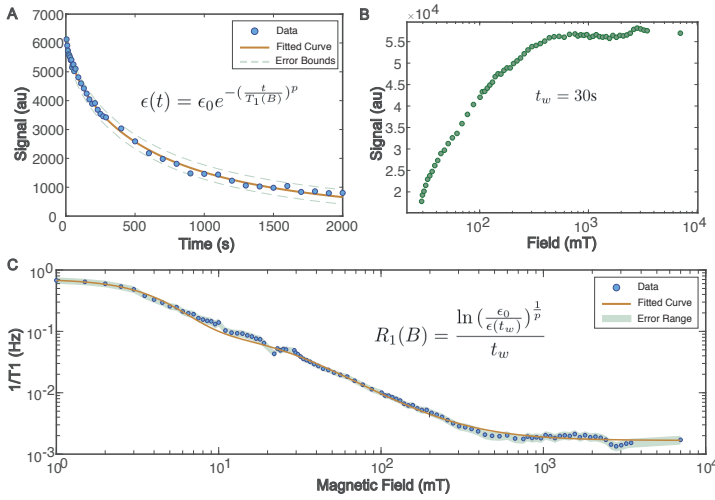


Figure S4. **Data processing.** (A) Spin polarization decay curves are acquired by repeated hyperpolarization of the diamond sample followed by time-dependent relaxation at a given field. By varying wait time and measuring the resulting NMR signal, relaxation parameters at this field can be estimated by fitting the data to a stretched exponential function. Because the relaxation rate equation incorporates a phenomenological stretch factor to account for T_1 heterogeneity at different fields, decay experiments are done at varied fields and the fitted parameters are used for different field regimes. (B) enhancement data is also taken at varying fields with wait time kept constant, providing a 1D slice of the relaxation dynamics at wide field ranges. To maximize signal contrast the wait times can be dynamically adjusted to account for particularly smaller relaxation times at lower fields. (C) Using the two previous experiments, a relaxation field map is constructed using the estimated rate equation parameters and the 1D enhancement data. Errors result from the quality of the decay curve fits and inaccuracies in the measured magnetic field.

allows greater flexibility in representing the relaxation rate as a function of field. Additionally our model assumes a constant offset to account for the saturation of the relaxation rate at high field, with functional form of a single Tsallian with respect to field B ,

$$R_1(B) = C_1 \left[1 + (2^{q-1} - 1) \left(\frac{B}{C_2} \right)^2 \right]^{-\frac{1}{q-1}} + C_3 \quad (7)$$

where fitting parameters C_1, C_2, C_3 describe the amplitude, width and vertical offset of the function respectively, and q regulates the effective contribution of the function's tail to the overall area under the function, with pointwise limits $q = 1$ and $q = 2$ denoting Gaussian and Lorentzian functions respectively. Originally the fitting models were limited to either Lorentzian/Gaussian line-shapes, and the model was susceptible to deviate from the experimental relaxation estimates at high field. By allowing variation of the parameter q , qualitatively better fits to the relaxation profiles can be found and analyzed in relation to one another.

B. Accelerated data collection strategy

We describe here an ‘‘accelerated technique’’ for data acquisition that we employ in experiments for long- T_1 samples. We work on the principle that one does not necessarily have to obtain the entire relaxation curve (with substantial time costs) in order to accurately measure the relaxation rates. Instead, employing an appropriate (stretched exponential) model, and with the measure-

ment of signal losses at fixed selections of waiting times allows the relaxation rates to be reconstructed with low error.

To be more precise, consider that due to long relaxation times at high field, occasionally approaching ~ 20 minutes, production of enhancement decay data at an array of magnetic fields is time-intensive. In order to hasten measurement times, and to obtain a denser map of nuclear T_1 estimates at a large number (~ 100) of field points (for example in Fig. 3), after hyperpolarization and subsequent transfer to the field of interest, the signal $\varepsilon(t_w)$ after some fixed wait time t_w (typically 30s) is measured. Fig. S4 details the procedure and benchmarks it. Indeed, the sample decay is field-dependent, and the set of enhancement values obtained in this manner allows a quantification of the the relaxation mechanisms throughout the full field range. To estimate T_1 from this data, however, requires knowledge of the enhancement generated before relaxation begins. To estimate this quantity, hereafter referred to as ε_0 , decay curves are experimentally acquired at certain fields using several averages per experiment, ensuring low error when fitting this curve to a stretched exponential model. Using the fit parameters T_1 and p , ε_0 can then be estimated as

$$\varepsilon_0 = \varepsilon(t_w) e^{\left(\frac{t_w}{T_1} \right)^p} \quad (8)$$

This estimate allows us to reconstruct the relaxation rate at each field for which enhancement measurements were acquired. Importantly, this process removes the need to construct a decay curve like that seen in Fig. S4A for each point of interest. Instead, decay curves for a subset of the field points can be found and the fit parameters from those curves can be used to approximate the relaxation rate for the points in Fig. S4B where an explicit decay curve is not created. By reordering the relaxation equation, the estimate of R_1 at field B becomes

$$R_1(B) = \frac{\ln \left[\frac{\varepsilon_0}{\varepsilon(t_w)} \right]^{\frac{1}{p}}}{t_w} \quad (9)$$

The quality of this reconstruction is improved by generating multiple decay curve experiments at varying fields so that the appropriate initial enhancements ε_0 and stretch factors p can be determined for different field regimes. For the two natural abundance ^{13}C samples in Fig. 3 (Samples 1-2 in Table I) we used decay curve data at fields of 20 mT, 35 mT, 150 mT, and 7 T for the relaxation field map reconstructions, with stretch factors $p \approx 0.75$ at lower fields and $p \approx 1$ at high fields. For the enriched samples in Fig. 5 (Samples 5-7 in Table I), the approximation method was used for the 3% sample whereas the other sample data was acquired using the longer 2D decay curve procedure.

In certain cases, especially for the ultralow field data in Fig. 3, rather than using a constant decay time t_w for all points, the sensitivity of the decayed enhancement readings is maximized by using *dynamically* varied wait times t_w at different fields; the loss in enhancement then becomes approximately 50% of the initial polarization value. This process mitigates errors in the measured enhancement values by creating sufficient contrast between the initial and decayed enhancement values, without excessively diminishing the signal relative to the noise.

Let us now quantify the time savings resulting from this data collection strategy. By removing the need to explicitly plot the signal decay over time at every magnetic field point, the effective dimensionality of our $T_1(B)$ measurement process is reduced, which allows determination of T_1 at a large number of field points rapidly. To develop an intuition for the accelerated in the averaging time gained as a result, we assume an even sampling of

the signal decay, in time increments Δt across n steps. To obtain estimates of T_1 at N field values, this would require at the very least a total time $t_{2D} = N\Delta t \sum_i^n i = N\Delta t \frac{n(n+1)}{2}$. While employing the accelerated 1D measurement strategy in contrast, signal enhancement is measured after a fixed wait time t_w at each field. These measurements are obtained at all N field points, after sampling with high accuracy the signal decay curves at N_d overlapping fields to construct estimates of the initial enhancement and stretch factor at varied fields. The experiment would therefore expend a minimum time of $t_{1D} = Nt_w + N_d\Delta t n(n+1)/2$. This measurement strategy incurs a theoretical time gain of $\frac{t_{2D}}{t_{1D}} = \frac{N\Delta t n(n+1)}{2Nt_w + N_d\Delta t n(n+1)}$, with the simplifying assumption that zero time is spent moving between fields as well as during signal detection. To demonstrate the possible time gains of this method, assume signal decay measurements at $\Delta t = 10$ s increments for a total of $n = 40$ points in time, across $N = 100$ field points. This may then be compared to the accelerated 1D measurement strategy, with signal enhancement measurements after a fixed hyperpolarization time of $t_w = 30$ s at each field. If $N_d = 4$ decay curves are used to estimate the relevant relaxation properties at four separate fields, the time gain of the 1D strategy is $\frac{t_{2D}}{t_{1D}} \approx 23$.

C. Error estimates

Let us now outline the error estimation in the $T_1(B)$ data. The primary sources of error come from the tightness of the decay curve fits to estimate ε_0 and p at different fields, the shot-to-shot error in the measured enhancement, and the error in the wait time spent relaxing at a given field. Because of the high averaging done to generate relaxation decay curves, the error in ε_0 and p , taken from the fitting function confidence intervals, is very small $\approx 1\%$. To account for variation in the relaxation wait time, the two methods used for placing the sample at a given field are considered. To access high field points the sample is shuttled into the magnet and allowed to wait a set time, and the error in this process arises from the shuttling time. Because the field cyclor can shuttle the sample over the maximum field range in less than 1 second, the shuttling error is approximated as 2 s. To access the low field regime, a bidirectional Helmholtz coil was assembled within the hyperpolarizer which is aligned with the field produced by the superconducting magnet in the $+z$ direction. This allows us to probe fields lower than what is covered by the field cyclor. At the polarization location and with no current driven through the coil, the 7T magnet produces a field of 20.8 mT, but fields as low as 1 mT and even further can be attained with use of the coil. To account for the build-up of magnetic field due to the coil, we attribute an error of 2s to all points found by this process. In combining both shuttled and coil-generated field points there was a constant offset of 15 mT added to all shuttled field points to make the curves consistent with the low field relaxation rate points.

IV. MODEL FOR HYPERPOLARIZED RELAXOMETRY

We now provide more details of the model employed to capture the relaxation mechanisms probed by our experiments. We had identified from the experiments three relaxation channels that are operational at different field regimes, driven respectively by (i) couplings of the ^{13}C nuclei to pairs (or generally the reservoir) of P1 center, (ii) individual P1 or NV centers, and (iii) due to spin-diffusion effects within the ^{13}C reservoir. In this section, we

detail lattice calculations that allow the estimation of the spectral densities in each of these cases.

Consider again the three disjoint spin reservoirs in the diamond lattice, the electron spin reservoir of NV centers, electron reservoir of substitutional-nitrogen (P1 centers), and the ^{13}C nuclear spin reservoir. They are centered respectively at frequencies $\omega_{\text{NV}} \approx [(\Delta \pm \gamma_e B_{\text{relax}} \cos \vartheta_{\text{NV}})^2 + (\gamma_e B_{\text{relax}} \sin \vartheta_{\text{NV}})^2]^{1/2}$, $\omega_e \approx [(\gamma_e B_{\text{relax}} + m_I A_{\parallel}^{\text{P1}} \cos \vartheta_{\text{P1}})^2 + (m_I A_{\perp}^{\text{P1}} \sin \vartheta_{\text{P1}})^2]^{1/2}$ and the nuclear Larmor frequency $\omega_L = \gamma_n B_{\text{relax}}$; where $\vartheta_{\text{NV}}, \vartheta_{\text{P1}}$ are angles of the NV(P1) axes to the field, $A_{\parallel}^{\text{P1}} \approx 114$ MHz, $A_{\perp}^{\text{P1}} \approx 86$ MHz are the hyperfine field of the P1 center to its host ^{14}N nuclear spin, $m_I = \{-1, 0, 1\}$ is the ^{14}N manifold, $\Delta = 2.87$ GHz is the NV center zero field splitting, and $\gamma_e = 28$ MHz/G and $\gamma_n = 1.07$ kHz/G are the electronic and nuclear gyromagnetic ratios.

A. Lattice estimates for electron reservoir

In order to determine the relaxation in behavior Eq. (3) quantitatively, let us determine typical inter-spin couplings and distances for the electron reservoir from lattice concentrations. First, for the electronic spins, given the relatively low concentrations, and the fact that the lattice is populated independently and randomly, we make a Poisson approximation following Ref. [35]. An estimate for the *typical* inter-spin distance $\langle r_e \rangle$ is obtained by determining the distance at which the probability of finding zero particles is $\frac{1}{2}$. Given the lattice spacing in diamond $a = 0.35$ nm, and the fact that there are four atoms per unit cell, we can estimate the electronic concentration in inverse volume units as, $N_e = (4 \times 10^{-6} P_e) / a^3$ [m^{-3}]. Then from the Poisson approximation $\langle r_e \rangle = (3/4\pi \ln 2)^{1/3} N_e^{-1/3}$ we obtain, for instance, $\langle r_{\text{NV}} \rangle = 12.12$ nm and $\langle r_{\text{P1}} \rangle = 2.61$ nm, where we have assumed concentrations of 1 ppm and 100 ppm respectively.

The inter-spin distances now allow us to calculate the second moment of the electronic spectra, which are reflective of the mean inter-spin couplings. Following Abragam [48], we have

$$M_{2e} = \frac{9}{20} (g\mu_B)^2 \frac{1}{\langle r_e \rangle^6}, \quad (10)$$

where $g \approx 2$ is the electron g-factor, and $\mu_B = 9.27 \times 10^{-21}$ erg/G the Bohr magneton in cgs units. Substituting this leads to, $M_{2e} = 43.65 P_e^2$ [mG^2], and allows us to estimate the electronic line width, $\Delta f_e = \langle d_{ee} \rangle \approx \gamma_e \sqrt{\frac{8}{\pi}} \sqrt{M_{2e}}$ [Hz] $\approx 10.5 P_e$ [mG], that scales approximately linearly with electron concentration P_e . Here we have assumed a Lorentzian lineshape and quantified the linewidth from the first derivative [35]. Typical values are $\Delta f_{\text{NV}} = 29.52$ kHz and $\Delta f_{\text{P1}} = 2.95$ MHz at 1 ppm and 100 ppm concentrations respectively.

Let us now estimate the effective hyperfine interaction from the P1 centers to the ^{13}C reservoir. Our estimate can be accomplished by sitting on a P1 spin, and evaluating the mean perpendicular hyperfine coupling that contributes to the spin flipping noise, $\langle A_{zx} \rangle = [\langle A_{zx}^2 \rangle]^{1/2}$, where we setup the second moment sum,

$$\langle A_{zx}^2 \rangle = \frac{1}{N} \left[\frac{\mu_0}{4\pi} \gamma_e \gamma_n \hbar \right]^2 \sum_j \frac{(3 \sin \vartheta_j \cos \vartheta_j)^2}{r_j^6} \quad (11)$$

where N is the total number of ^{13}C spins for every P1 center and ϑ_j is the angle between the P1- ^{13}C axis and the magnetic field. Numerically the factor $\frac{\mu_0}{4\pi} \gamma_e \gamma_n \hbar = 19.79$ [kHz (nm) 3]. For simplicity, we can approximate the sum by an integral, and including

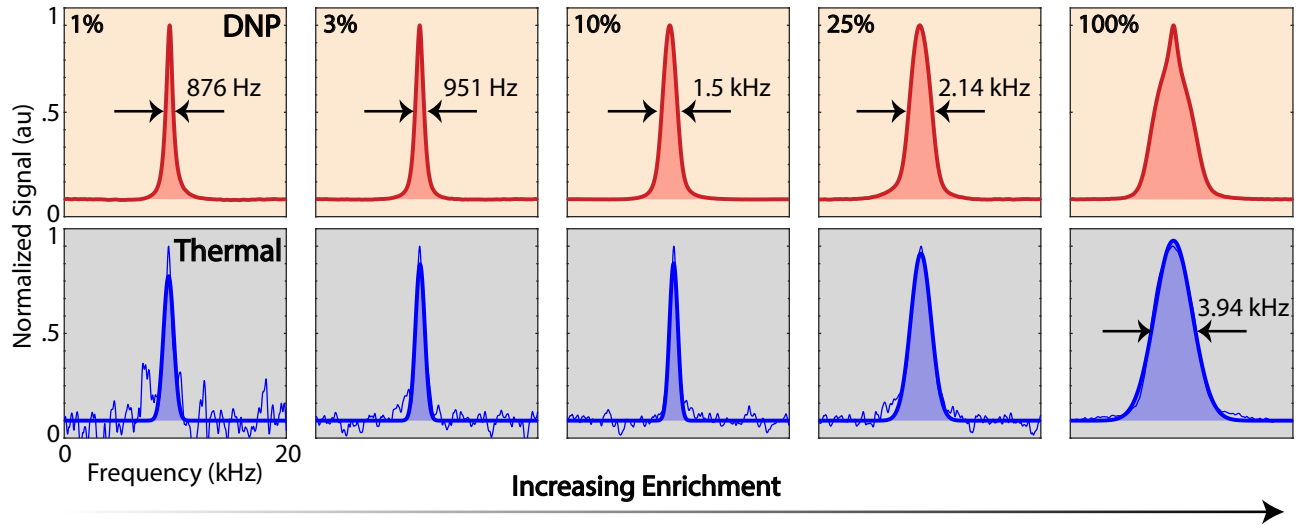


Figure S5. **Comparison of DNP and thermal ^{13}C lineshapes.** Panels indicate lineshapes under (A) hyperpolarization carried out at low field (1-30 mT) and (B) 7 T thermal polarization. DNP is excited from the optically polarized NV centers which are ≈ 1 ppm in all samples. For the 100% sample, we ascribe the broad and narrow components of the lineshapes (dashed lines) as being spins close and further away from the NV centers respectively. The scaling of the experimental linewidths matches our predictions from theory (see Fig. S6C).

the density of ^{13}C spins $N_C = 0.92\eta$ spins/nm 3 (see Fig. S6B), where η is the ^{13}C enrichment level,

$$\langle A_{zx}^2 \rangle = \left(\frac{\mu_0}{4\pi} \gamma_e \gamma_n \hbar \right)^2 \frac{N_C (2\pi)}{N_C \mathcal{V}} \int_{r_0}^{\langle r_e \rangle} \int_0^{\pi/2} \frac{(9 \sin^3 \vartheta \cos^2 \vartheta)}{r^6} r^2 dr d\vartheta$$

where $\mathcal{V} = \frac{4\pi}{3} \langle r_e \rangle^3$ corresponds to the volume of spins considered. We have assumed that the “sphere of influence” of a particular P1 spin notionally extends to the mean distance between neighboring P1 centers, for instance $\langle r_e \rangle = 5.62$ nm for $P_e = 10$ ppm. The integral lower limit is set by the requirement that the hyperfine shift of the ^{13}C nuclei is within the detected NMR linewidth $\Delta f_{\text{det}} \approx 2$ kHz. Then, $r_0 = [19.79 / (\Delta f_{\text{det}})]^{1/3} \approx 2.15$ nm. In principle, r_0 goes to quantify a “barrier” around each P1 center, wherein the hyperfine interactions prevent the ^{13}C nuclei from being directly observable in our relaxometry experiments. The angle part of the integral evaluates to $6/5$, and effectively therefore,

$$\langle A_{zx}^2 \rangle = \left(\frac{\mu_0}{4\pi} \gamma_e \gamma_n \hbar \right)^2 \frac{6}{5} \frac{1}{\langle r_e \rangle^3} \left(\frac{1}{r_0^3} - \frac{1}{\langle r_e \rangle^3} \right) \quad (12)$$

For instance, for the two natural abundance single crystal samples that we considered in the Fig. 3 of the main paper with P1 concentration 17 ppm and 48 ppm, we have $\langle r_e \rangle = 4.8$ nm and 3.39 nm respectively, giving rise to the effective P1- ^{13}C hyperfine interaction $\langle A_{zx}^2 \rangle \approx 0.39$ [(kHz) 2] and $\langle A_{zx}^2 \rangle \approx 0.45$ [(kHz) 2] respectively. The simple model predicts that the effective hyperfine coupling increases slowly with the electron concentration P_e , that the electron spectral density width $\langle d_{ee} \rangle \propto P_e$. It also shows that the electron spectral density is independent of ^{13}C enrichment η to first order. The zero-field relaxation rates stemming from this coupled-electron mechanism can now be calculated as $R_1(0) = \langle A_{zx}^2 \rangle / \langle d_{ee} \rangle \approx 777$ [s $^{-1}$] and 317.5 [s $^{-1}$]. This matches our expectation for the order of magnitude of the zero field rate since we expect that the ^{13}C relaxation time T_{1n} matches that of the electron $T_{1e} \approx 1$ ms.

In order to validate the conclusions from this simple model, we perform an alternative numerical estimation of $\langle A_{zx}^2 \rangle =$

$\left[\frac{1}{N} \sum_{j \in \Delta f_{\text{det}}} \langle A_{zx,j}^2 \rangle \right]$ within the detection barrier directly from the diamond lattice (see Fig. S6F and Sec. IV C). We obtain $\langle A_{zx}^2 \rangle = 2$ [(kHz) 2] and 2.26 [(kHz) 2] for Samples 1 and 2 respectively, in close and quantitative agreement with the values predicted from Eq. (12) (considering the approximations made in the analysis). Numerics also confirm that the hyperfine values $\langle A_{zx}^2 \rangle$ are independent of enrichment η (see Fig. S6F) in agreement with the experimental data.

B. Lattice estimates for ^{13}C reservoir

In contrast, since the ^{13}C reservoir has a much larger spin density, especially at high enrichment levels, we will estimate the interspin distances $\langle r_n \rangle$ and couplings Δf_n numerically. The experimentally obtained ^{13}C lineshapes and resulting linewidths for all the samples considered are shown in Fig. S5. We begin by first setting up a diamond lattice numerically and populating the ^{13}C spins with enrichment level set by η . The numerical calculation is tractable since only small lattice sizes typically under $\ell = 10$ nm are sufficient to ensure convergence of the various dipolar parameters (see Fig. S6A). To a good approximation, we determine the spin density of the ^{13}C nuclei to be $N_C = 0.92\eta$ spins/nm 3 (see Fig. S6B). Next, in order to determine the nuclear dipolar linewidths, we consider the secular dipolar interaction between two nuclear spins j and k in lattice,

$$d_{jk}^{\text{CC}} = \frac{\mu_0}{4\pi} \hbar \gamma_n^2 (3 \cos^2 \vartheta_{jk} - 1) \frac{1}{r_{jk}^3} \quad (13)$$

where $\vartheta_{jk} = \cos^{-1} \left(\frac{\mathbf{r}_{jk} \cdot \mathbf{B}_{\text{pol}}}{r_{jk} B_{\text{pol}}} \right)$ is the angle between the inter-nuclear vector and the direction of the magnetic field. In the numerical simulations we will consider, we evaluate the case of single crystal samples placed flat, i.e. with $\mathbf{B}_{\text{pol}} \parallel [001]$ crystal axis. As a result, for ^{13}C spins on adjacent lattice sites, $\vartheta_{jk} = 54.7^\circ$ is the magic angle and $d_{jk}^{\text{CC}} = 0$. We note that Eq. (13) is a good approximation even *during* the hyperpolarization process. Indeed, although hyperpolarization is performed in the regime where the

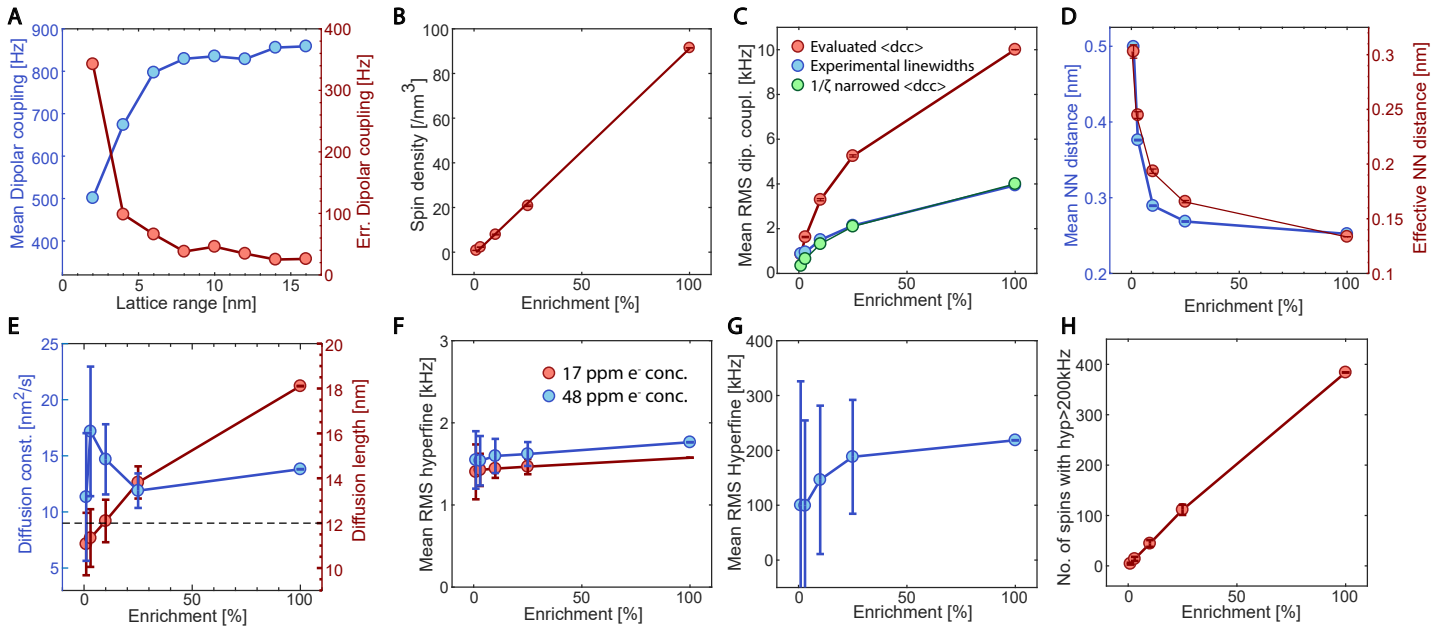


Figure S6. Calculated interspin parameters pertaining to ^{13}C and NV reservoirs as a function of lattice enrichment η . (A) Convergence of numerical estimates is representatively illustrated by plotting the mean ^{13}C dipolar coupling $\langle d_{CC} \rangle^\ell$ and the residual $\epsilon(\ell)$ as a function of considered lattice size ℓ . We evaluated here the case of a 1% enriched diamond single crystal. We observe good convergence beyond a lattice size of about 10 nm. (B) Spin density of ^{13}C nuclei shows, as expected, very close to linear dependence with η . Solid line is a linear fit, whose slope returns the lattice spin density $\approx 0.92\eta$ spins/nm 3 . (C) Effective inter-nuclear dipolar coupling $\langle d_{CC} \rangle$ evaluated from second moment (red line). Blue points show the experimentally obtained linewidths. Green line indicates $\frac{1}{\zeta} \langle d_{CC} \rangle$ with broadening factor $\zeta = 2.5$, and shows a good numerical agreement with experimental data. (D) Mean inter-spin distance $\langle r_n \rangle$ between lattice ^{13}C nuclei in evaluated from the RMS dipolar coupling (red points) and from effective nearest-neighbor lattice distances (blue points). The two estimates show a good match, with the inter-spin distance falling approximately as $\eta^{1/3}$. (E) Diffusion constant and diffusion length numerically estimated with lattice enrichment. Here we employed experimentally obtained values of ^{13}C T1. Dashed line indicates the mean inter-electron distance between NV centers at 1ppm concentration, indicating that spin diffusion can homogeneously spread polarization in the lattice almost independent of ^{13}C enrichment. (F) Effective hyperfine coupling $\langle A_{zx}^{\text{obs}} \rangle$ to P1 centers in case of single crystal samples with 17 ppm (red points) and 48 ppm (blue points) electron concentration. Results indicate that $\langle A_{zx}^{\text{obs}} \rangle$ is independent of ^{13}C enrichment η . (G) Estimates of mean RMS NV- ^{13}C hyperfine interaction $\langle A_{NV} \rangle$ with lattice enrichment. (H) Estimation of directly participating ^{13}C nuclei in the DNP process, defined as those nuclei for which the hyperfine coupling to the closest NV center is greater than 200 kHz. We obtain an approximately linear increase with enrichment. Error bars in all panels are numerically estimated from standard deviation of lattice parameter distributions over several realizations of the lattice configuration.

nuclear Larmor frequency ω_L is smaller than the hyperfine interaction A to the NV center, the hyperfine field is only transiently on during the microwave sweep. Given the fact that the NV center is a spin-1 electron, there is no hyperfine field applied to the nuclei when the NV is optically pumped to the $m_s = 0$ spin state. Indeed this constitutes the majority of time period of the DNP process.

We now evaluate the effective mean dipolar coupling $\langle d_{CC} \rangle$ between the nuclei from the second moment,

$$\langle d_{CC} \rangle = \frac{1}{N} \sum_j \left[\sum_k \left(\frac{\mu_0}{4\pi} \hbar \gamma_n^2 (3 \cos^2 \vartheta_{jk} - 1) \right)^2 \frac{1}{r_{jk}^6} \right]^{1/2}, \quad (14)$$

where $N = N_C \ell^3$ refers to the number of ^{13}C spins in the lattice, and for the convergence, we assign for simplicity, $1/r_{jj}=0$. This simply allows us to sum over all the spins j in the lattice. In practice, we evaluate the parameter $\langle d_{CC} \rangle$ in Eq. (14) over several (≈ 20) realizations of the lattice and take an ensemble average (see Fig. S6C). We report an effective error bar from the standard deviation of this distribution. The fidelity of the obtained results is evaluated by testing the convergence $\epsilon(\ell) = \|\langle d_{CC} \rangle^{\ell+1} - \langle d_{CC} \rangle^\ell\|$, where the $(\ell + 1)$ superscript indicates a lattice expanded by 1nm. As is evident in the representative example for $\eta = 1.1\%$ displayed in Fig. S6A, we find good

convergence ($\epsilon \rightarrow 0$) for $\ell \approx 14$ nm, corresponding to about 2500 lattice ^{13}C nuclei.

It is instructive to now compare the estimated values with the experimentally determined nuclear linewidths $\Delta f_n(\eta)$ measured at 7 T (see Fig. S5 and blue points in Fig. S6C). The scaling (solid line in Fig. S6C) of the experimental data $\sim \eta^{1/2}$ matches closely with the estimated result through Eq. (14) (see red line in Fig. S6C). However we find that the numerical value overestimates the linewidth by an additional broadening factor $\zeta \approx 2.5$. The green points show a close match between experimental values and numerically evaluated $\frac{1}{\zeta} \langle d_{CC} \rangle$.

This effective coupling now allows us to estimate the mean inter-spin distance $\langle r_n \rangle$ as a function of ^{13}C enrichment (see Fig. S6D),

$$\langle r_n \rangle = \left[\frac{2 \langle d_{CC} \rangle}{\frac{\mu_0}{4\pi} \gamma_n^2 \hbar} \right]^{-1/3} \quad (15)$$

We find a scaling $\sim \eta^{-1/6}$ (red line in Fig. S6D). It is also interesting to compare these values to those alternatively evaluated directly from the lattice (blue points in Fig. S6C). For this, we rely on the fact that the $\langle r_n \rangle$ distances largely reflect the nearest-neighbor (NN) spin distances. We define the NN spin (say k) to the spin j as the one which has the dipolar coupling d_{jk} is maxi-

mal. Now for every spin j in the lattice, we determine the nearest neighbor inter-spin distance $R_j = |r_{jk}^{\text{NN}}|$, and construct a row matrix, $\mathbf{R} = \{R_j\}$, with j^{th} element R_j . Finally, repeating and concatenating this row matrix for several realizations of the lattice, we finally estimate $\langle r_n \rangle = \langle \mathbf{R} \rangle$ for the i^{th} realization of the lattice. The comparison between these two metrics is demonstrated in Fig. S6D), and show reasonably good agreement.

These inter-spin distances and the coupling values allow us to estimate the spin diffusion coefficient $D(\eta)$ as a function of lattice enrichment (see Fig. S6E). This quantifies the spread of polarization away from directly polarized ^{13}C nuclei, and also serves as a means to quantify the homogenization of polarization in the lattice. Following Ref. [53], we heuristically assign a spin diffusion coefficient $D = \frac{\langle r_n \rangle^2}{30T_{2n}}$ where the T_{2n} are evaluated here by only taking the dipolar contribution to the linewidth, $T_{2n} \approx 1/\langle d_{CC} \rangle$. Given a total time bounded by T_1 , we can calculate the rms overall diffusion length [54] as $\sigma = \sqrt{2DT_1}$ that is displayed as the blue points in Fig. S6D. Also for reference is plotted the mean NV-NV distance ≈ 12 nm at 1 ppm concentration, indicating that to a good approximation that the optically pumped polarization reaches to all parts of the diamond lattice between the NV centers.

C. Lattice estimates for hyperfine couplings to NV and P1 reservoirs

Let us finally evaluate, through similar numerical means, details of the hyperfine interaction between ^{13}C reservoir and the electron reservoirs of the P1 centers and NV centers. We draw a distinction between the NV and P1 centers in the fact that the former are spin-1, with a nonmagnetic $m_s = 0$ state (with no hyperfine coupling to first order), while the latter are spin 1/2. When hyperfine shifts exceed the observed 7 T NMR linewidth $\Delta f_{\text{det}} \sim 2$ kHz, it is safe to assume that these spins are unobservable - a case that is operational more strongly for the spin 1/2 P1 centers.

In order to perform the estimation, in the generated lattice of size $\ell = \langle r_e \rangle$, we populate ^{13}C spins with enrichment η , and include an electron at the lattice origin. The mean perpendicular hyperfine interaction between P1- ^{13}C spins is calculated from the second moment, from the individual hyperfine couplings $A_{zx,j}$ that are smaller than the detection barrier Δf_{det}

$$\begin{aligned} \langle A_{zx}^{\text{obs}} \rangle &= \left[\sum_{j \in \text{obs}} \langle A_{zx,j}^2 \rangle \right]^{1/2} \\ &= \left[\frac{1}{N_{\text{obs}}} \sum_{j \in \text{obs}} \left(\frac{\mu_0}{4\pi} \gamma_e \gamma_n \hbar \right)^2 \frac{(3 \sin \vartheta_j \cos \vartheta_j)^2}{r_j^6} \right]^{1/2} \end{aligned}$$

where N_{obs} refers to the number of spins amongst the total $N = N_C \ell^3$ spins for which $\langle A_{zx,j}^2 \rangle < (\Delta f_{\text{det}})^2$. Here r_j is the distance of the j^{th} ^{13}C nucleus, and ϑ_j the angle of P1- ^{13}C axis to the magnetic field, and we have ignored the effect of ^{14}N hyperfine interactions intrinsic to the P1 center. This effective hyperfine field, scaling with lattice enrichment η , is then indicated by the red (blue) points in Fig. S6F for electron concentrations of 17 ppm (48 ppm) respectively. The error bars indicating the standard deviation of the obtained distributions upon several hundred realizations of the lattice. We observe that the effective hyperfine interaction $\langle A_{zx}^{\text{obs}} \rangle$ is almost independent of η , and is higher for lattices with higher P_e electron concentration. This is consistent with the results obtained through Eq. (12) and matches our experimental observations in Fig. 5 of the main paper. For natural abundance samples we numerically obtain $\langle A_{zx}^{\text{obs}} \rangle = 1.4$ kHz, 1.55 kHz, and 1.04 kHz respectively for 17 ppm, 48 ppm, and 1 ppm (representative of NV center concentrations), in agreement with estimates from Eq. (12).

Finally, let us estimate the number of spins that are directly polarized by the NV centers. In Fig. S6G we evaluate the *full* hyperfine interaction to ^{13}C spins of varying enrichment, considering no operational detection barrier.

$$\begin{aligned} \langle A_{\text{NV}} \rangle &= \left[\sum_j \langle A_{j,\text{NV}}^2 \rangle \right]^{1/2} \\ &= \left[\frac{1}{N} \sum_j \left(\frac{\mu_0}{4\pi} \gamma_e \gamma_n \hbar \right)^2 \frac{[(3r_{jz}^2 - 1)^2 + (3r_{jx}r_{jz})^2 + (3r_{jy}r_{jz})^2]}{r_j^6} \right]^{1/2} \end{aligned}$$

where we employed a lattice size $\ell = \langle r_{\text{NV}} \rangle = 12$ nm, and $N = N_C \ell^3$ refers to the number of ^{13}C spins in the lattice with index j running over all them. Here the angle part of the hyperfine interaction is evaluated by assigning the direction cosines, for instance as, $r_{jz} = (\vec{r}_j \cdot \hat{z}_{\text{NV}})/r_j$, where \hat{z}_{NV} is the unit vector aligned along the N-V axis, collinear with the direction of the strong zero field splitting that forms the dominant part of the Hamiltonian at low fields. This effective hyperfine field, scaling with lattice enrichment η , is then indicated by the blue points in Fig. S6G. Our DNP mechanism is a low-field one and is primarily effective when the full hyperfine coupling $\langle A_{j,\text{NV}} \rangle$ is of the order of greater than the nuclear Larmor frequency $\omega_L = \gamma_n B_{\text{pol}}$, where B_{pol} is the polarizing field. We can heuristically measure the number of directly polarized spins surrounding an NV center as being those for which $\langle A_{j,\text{NV}} \rangle > 200$ kHz. As Fig. S6H indicates, the number of such directly polarized nuclei scales approximately linearly with ^{13}C enrichment, with a constant ratio $\approx 4.3\eta$ in the diamond lattice. Spin diffusion therefore plays an important role in the spread of polarization away from these directly polarized nuclei.